Experimental Validation of a Spatial Anti-aliasing Plasma Wave Analysis Technique on Ion Acoustic Turbulence in a Hollow Cathode Plume

IEPC-2025-357

Presented at the 39th International Electric Propulsion Conference, Imperial College London, London, United Kingdom
14-19 September 2025

Miron F. Liu* and Benjamin A. Jorns†
University of Michigan, Plasmadynamics and Electric Propulsion Laboratory, Ann Arbor, MI, 48109

An anti-aliasing analysis technique for inferring wave dispersion leveraging multi-point correlation and Bayesian inference is experimentally validated on ion acoustic turbulence in a hollow cathode plume. The theoretical underpinnings of the algorithm are presented as well as the experimental setup, which consists of a 20-A class LaB6 hollow cathode and a pair of ion saturation probes capable of in-situ adjustment of probe angle and spacing. Dispersion plots produced by the spatial anti-aliasing framework are compared against Beall plots, which are constructed with conventional two-point correlation. The results highlight the robust anti-aliasing properties of the algorithm and suggest that this technique may be employed to extend the spectral bandwidth of plasma wave diagnostics to wavelengths on the order of the probe diameter (≈ 0.5 mm) by eliminating aliasing of dispersion data due to the finite separation of probe elements. This methodology thus makes possible the experimental detection of small length-scale instability modes of interest existing at wavelengths between 0.5 mm and 3 mm that are of interest in this device, and in similar crossed-field, low-temperature plasma systems, such as the modified two-stream instability and lower hybrid drift instability.

I. Introduction

The gradient-rich, flowing plasma environments of many electric propulsion (EP) devices are conducive to the onset and growth of various plasma instabilities. These waves are believed to manifest numerous deleterious effects, including reduced device efficiency and, more critically, accelerated erosion of thruster surfaces such as the pole erosion observed on magnetically shielded Hall thrusters [1][2]. Given that these waves have been shown to influence electron and ion dynamics in EP plasmas, it is important to incorporate them into models to rigorously account for their impact on device performance and lifetime. Unfortunately, a comprehensive understanding of these modes and their exact relation to anomalous particle and energy transport, and thus impact on key erosion processes, within these devices has yet to be achieved.

This gap in understanding, in large part, stems from the limitations of current low-temperature plasma (LTP) wave diagnostics. Aliasing effects arising from the finite spacing between wave probe elements impose a lower bound on the wavelengths that physical probe-based methods can resolve [3]. In contrast, optical techniques for measuring wave properties, such as coherent Thompson scattering (CTS), have inherent *upper bounds* in spectral bandwidth [4][5]. Taken together, these restrictions have precluded direct experimental measurement of modes with wavelengths between 0.5 mm and 3 mm. Unfortunately, it is within this regime where key modes that are believed to be linked to anomalous erosion in certain EP devices achieve their theoretical maximum growth rates [6][7].

In light of these outstanding limitations, the authors recently numerically validated a spatial anti-aliasing technique that leverages multi-point correlation and Bayesian inference to reconstruct a de-aliased proba-

*PhD Candidate, Aerospace Engineering, mironliu@umich.edu
†Associate Professor, Aerospace Engineering, bjorns@umich.edu

Copyright 2025 by the Electric Rocket Propulsion Society. All rights reserved.

bility distribution function (PDF) of dispersion [8]. In principle, this framework expands the resolvable wavelength regime and thus allows experimental measurements of moderate-length scale modes existing in the previously inaccessible wavelength regime. However, while the anti-aliasing algorithm showed promise, the initial validation effort was purely numerical and modeled propagating plasma waves as idealized plane waves. While this simplicity is appropriate as a first-pass benchmark, allowing straightforward comparison between simulation outputs and known inputs, this approach does not fully capture the complexity of wave phenomena in real LTP environments. In such plasmas, wave propagation is not strictly periodic, wavevectors and amplitudes may vary spatially over length scales comparable to the probe spacing, and multiple plasma waves may concurrently propagate. There thus remains an apparent need to assess the performance of the algorithm under real experimental conditions.

We address this need in this work by experimentally validating the spatial anti-aliasing algorithm on the dispersion of ion acoustic turbulence in the plume of a hollow cathode. With this goal in mind, this paper is structured as follows: in Section II we overview the theory of ion acoustic waves. In Section III, we detail the analysis techniques we employ to extract salient wave properties from experimental data. Next, we describe our experimental arrangement in Section IV. We then present results in Section V, followed by a discussion of our findings in Section VI. Finally, in Section VII, we present a summary of the work and key conclusions.

II. Theory of Ion Acoustic Waves

The ion acoustic instability is an electrostatic wave mode that can spontaneously onset in plasma exhibiting large disparities in ion and electron temperatures and drift velocities [9]–[11]. These two conditions are met in the plume of hollow cathodes, and recent experimental efforts have confirmed the existence of such waves in these devices [3][12]. The theoretical framework for characterizing the presence and behavior of waves in plasma is the dispersion relation. This relationship for ion acoustic waves in the hollow cathode plasma can be derived from a linearization of the ion and electron fluid equations [3][13] subject to the simplifying assumptions characteristic of plasma parameters in a hollow cathode plasma: $|\vec{v_i}| \ll c_s \ll |\vec{v_e}| \ll v_{th_e}$, where $c_s = \sqrt{\frac{qT_e}{m_i}}$ is the ion sound speed, $v_{th_e} = \sqrt{\frac{qT_e}{m_e}}$ is the electron thermal speed, $\vec{v_i}$ is the ion drift velocity, $\vec{v_e}$ is the electron drift velocity. Here q, T_e, m_i, and m_e denote elementary charge, electron temperature, ion mass, and electron mass, respectively. The real part of the dispersion relation is given by [13]

$$\omega_{RE} = \frac{kc_s}{\sqrt{1 + k^2\lambda_{De}^2}} + \vec{k} \cdot \vec{v_i}, \tag{1}$$

where ω_{RE} denotes the real component of angular frequency, $\lambda_{De} = (\frac{\varepsilon_o T_e}{n_e q^2})^{1/2}$ is the electron Debye length, k is the wavenumber (spatial frequency of a mode), and $\vec{k}$ is the wave vector. Here ε_o and n_e denote the permittivity of free space and electron number density. Noting that the experimentally observed frequencies at which ion acoustic waves have been found to propagate at are lower than the ion plasma frequency [3], $\omega_{RE} \ll \omega_{pi} = (\frac{n_e q^2}{\varepsilon_o m_i})^{1/2}$, and at low wavenumbers, we may approximate Eq. 1 in the limit $\lambda_{De}k \ll 1$ as (c.f. [13])

$$\omega_{RE} = kc_s + \vec{k} \cdot \vec{v_i}. \tag{2}$$

By inspection of the first term on the right-hand side, it is evident that in the reference frame of the ions, these waves propagate at the ion-sound speed, whence they derive their name. The second term on the right-hand side of Eq. 2 represents a Doppler shift, i.e. a transformation of the wave speed from the ion frame into the lab frame. If we assume the ion drift velocity to be in the direction of wave propagation, the group velocity of the waves simply becomes the sum of the ion sound speed and drift velocity

$$v_g = \omega_{Re}/k = c_s + v_i. \tag{3}$$

To confirm the presence of IAT in a plasma, we experimentally measure wave dispersion and compare it against its theoretical form. We detail methods to experimentally obtain dispersion in the following section.

Copyright 2025 by the Electric Rocket Propulsion Society. All rights reserved.

III. Analysis methods for inferring wave properties

We present in this section two techniques for measuring the dispersion of waves. The first is two-point correlation, a conventional wave analysis method that infers wave dispersion from correlated measurements of plasma parameters, typically ion saturation current, between two spatially separated probes. The second is a new analysis method that leverages multiple data sets taken at various probe orientations (spacings and/or angles) through Bayesian inference to arrive at a de-aliased probability distribution of dispersion.

A. Inferring wave dispersion using two-point correlation

Inferring plasma wave dispersion requires a method to map the temporal frequency of a propagating mode to its spatial frequency, i.e. its wavelength or wavenumber. A common technique employed to perform this mapping - two-point correlation analysis - exploits the phase difference of a propagating plasma wave measured by two spatially disparate physical probes to infer its wavelength. To illustrate this technique, we show in Fig. 1 a notional schematic of the typical two-probe configuration and corresponding spectral data used to infer wave dispersion.

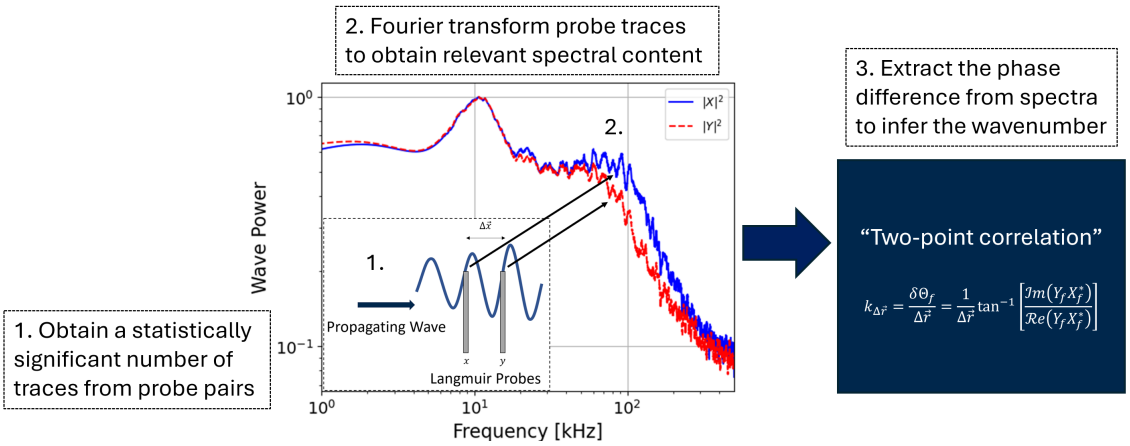

Figure 1: Notional diagram of two-probe correlation technique

As a first step, a pair of ion saturation probes (shown in the lower left in Fig. 1) is inserted into a plasma at two positions, x and y, which define a probe vector $\Delta\vec{r}$. As electrostatic waves propagate between the probe elements, the finite probe spacing introduces a phase difference, $\delta\Theta_f$, in the time-varying signal recorded at each location, $\tilde{\phi}(x,t)$ and $\tilde{\phi}(y,t)$, where $y = x + \Delta\vec{r}$. Following the formulation given in [3], the Fourier transforms of these signals, X_f and Y_f, respectively, can be manipulated to extract $\delta\Theta_f$ and thus solve for the wavenumber of propagating modes (wavenumber is proportional to inverse wavelength) $k_{\Delta\vec{r}}(f)$ along the axis connecting the two probe elements as a function of frequency f. Here, the superscript "$*$" denotes complex conjugated quantities.

$$k_{\Delta\vec{r}}(f) = \frac{\delta\Theta_f}{\Delta\vec{r}} = \frac{1}{\Delta\vec{r}}\tan^{-1}\left[\frac{\mathcal{I}m(Y_f X_f^*)}{\mathcal{R}e(Y_f X_f^*)}\right]. \tag{4}$$

In other words, given spectra measured at two probe locations and knowledge of the inter-probe spacing, Eqn. 4 allows length-scale information of the mode to be extracted from time-varying probe traces and mapped to frequencies, thus providing a framework for experimentally inferring plasma wave dispersion.

B. Binning two-point correlation measurements via Beall analysis

As noted in [3] and [14], two-point correlation is sensitive to noise and can be errant if multiple modes are present in the plasma, i.e. if there is more than one wavenumber at a given frequency. In light of this, we adopt the probabilistic approach of Beall et al. in which we first collect M samples of spectra, next evaluate wavenumber as a function of frequency according to Eq. 4 for each sample, and lastly apply a weighted binning of the wavenumber-frequency pairs according to

Copyright 2025 by the Electric Rocket Propulsion Society. All rights reserved.

$$S(f,k) = \frac{1}{M}\sum_{j=1}^{M} I_{0,\Delta k}[k^i - k^j(f)]\frac{1}{2}[P_1^j(f) + P_2^j(f)]. \tag{5}$$

Here S represents the "intensity", i.e. the weighted number of two-point correlation samples that fall within each bin. The index j denotes the sample number, i denotes the wavenumber index in the discretized domain, P_1 and P_2 are the power spectra of fluctuations measured at x and y, respectively, i.e. XX^* and YY^*, and $I_{0\Delta k}$ is an indicator function defined as

$$I_{0\Delta k} = \begin{cases} 1 & \text{if } |x| < \Delta k \\ 0 & \text{otherwise.} \end{cases} \tag{6}$$

By iterating through all sample j, frequencies f, and wavenumbers i, and applying the binning approach described by Eqns. 5 and 6 with $\Delta k = k^i - k^j(f)$ we construct a 2D histogram yielding S as a function of frequency and wavenumber. Larger values of S indicate frequency-wavenumber pairs that are dominant in the measurement domain.

C. Aliasing of dispersion obtained through two-point correlation

It is evident from Eqn. 4 that the principal limitation of two-point correlation analysis arises from the $[-\pi, \pi]$ range restriction of the arctan function. This restriction imposes a maximum resolvable wavenumber determined by the spacing of the probe element, $|k_{max}| \leq \pi/\Delta\vec{r}$, such that modes with wavenumbers greater than this limit are "phase-wrapped" into this interval. The result is aliasing: modes with sufficiently high wavenumber are subject to phase-wrapping and become indistinguishable from non-phase-wrapped, low wavenumber modes.

We illustrate how aliasing may manifest in experimental data in Fig. 2. Suppose we measure propagating plasma waves with a linear dispersion relation, typical of ion acoustic waves, given by Fig. 2a. We note that the uncharacteristically low group velocity (typically on the order of a few km/s) is exaggerated for demonstration purposes. Here we will assume a typical probe spacing of 4 mm but allow the smallest wavelength modes to extend well below 4 mm ($\gtrsim 800\ m^{-1}$). We may then use Beall analysis [14], a technique commonly used to bin two-point correlation results, for example, to generate a histogram of wave dispersion. This is notionally shown in Fig. 2b. We immediately see spatial aliasing in the dispersion plot, characterized by the multiple parallel striations stemming from the phase wrapping of modes with wavelengths smaller than the inter-probe spacing.

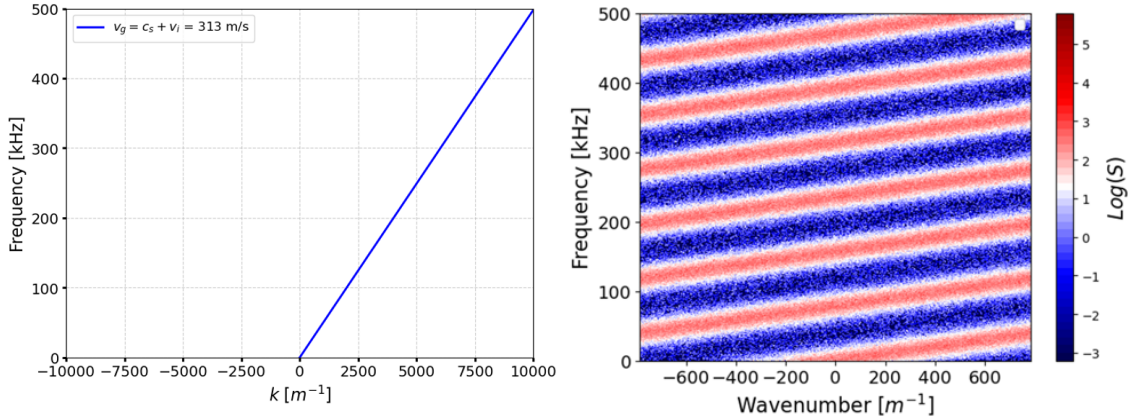

(a) (b)

Figure 2: Notional Example of Two-Point Correlation Technique Subject to Aliasing: a) True Dispersion b) Dispersion Inferred via Two-Point Correlation [8]

Jorns et al. demonstrated that these aliasing artifacts can be mitigated by leveraging the apparent periodicity of the phase-wrapped, experimentally measured dispersion to reconstruct a de-aliased dispersion plot [3].

Copyright 2025 by the Electric Rocket Propulsion Society. All rights reserved.

While this approach is effective at de-aliasing dispersion plots with simple, linear dispersion, as in the case of the aforementioned work, instabilities in other EP plasmas may exhibit nonlinear dispersion [15][16]. Furthermore, the manual de-aliasing technique is most effective when a single, dominant mode is present. However, multiple instabilities may coexist in a plasma. Dispersion features may overlap if none of the modes are sufficiently dominant. This, coupled with aliasing uncertainty, has made it challenging to apply this de-aliasing technique to nonlinear dispersion measurements in some EP devices [17].

D. Anti-aliasing algorithm

The anti-aliasing approach presented in this work is predicated on the principle that varying the probe spacing and/or angle produces a corresponding change in the phase delay measured by the probe pair that is unique to a propagating mode. This invites the possibility that measurements obtained across multiple probe geometries (i.e., distinct angle–spacing combinations) can be jointly analyzed through Bayesian inference to regress a probability distribution of the true wavenumbers. We give a brief overview of our anti-aliasing data framework here. Additional details on our Bayesian inference methodology are provided in our previous work [8].

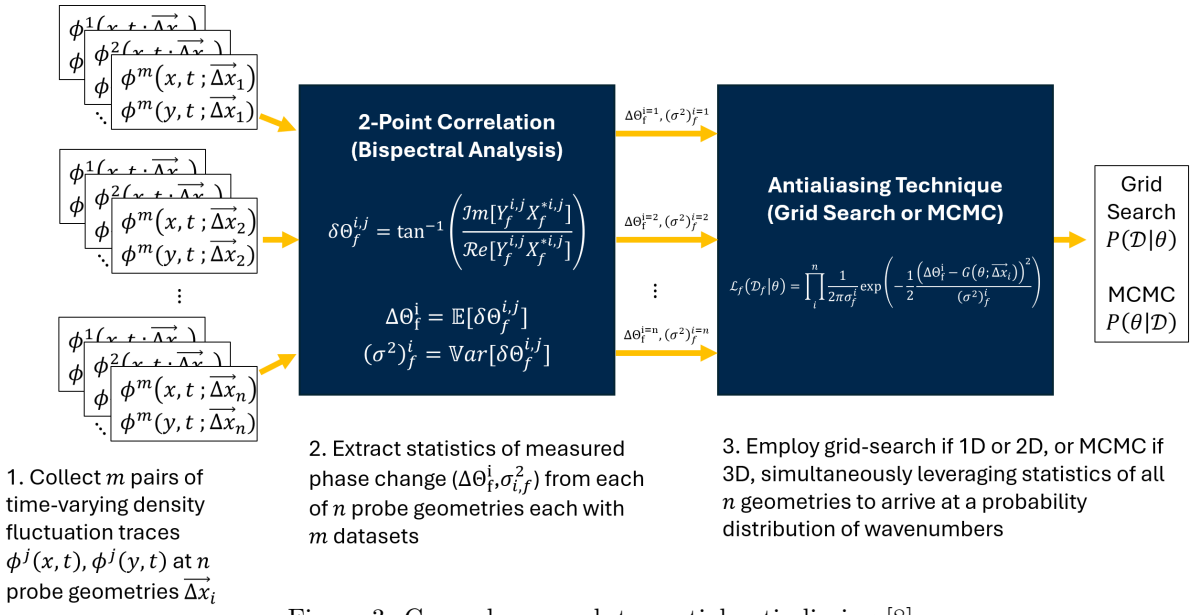

Figure 3: General approach to spatial anti-aliasing [8]

Fig. 3 illustrates schematically our anti-aliasing data analysis process. We begin by obtaining a statistically sufficient m number of time-varying probe-pair traces for each of n probe orientations. Next, we divide the frequency domain into F frequencies. For each frequency f and probe geometry $\Delta\vec{r}_i$, we generate a histogram using m samples of the measured phase difference, $\delta\Theta_f^i$, from which we extract the mean, $\Delta\Theta_f^i = \mathbb{E}[\delta\Theta_f^{i,j}]$, and variance $(\sigma^2)_f^i = \mathbb{V}ar[\delta\Theta_f^{i,j}]$. Here, samples are indexed by the superscript j and the probe geometries are indexed by the superscript i. Due to phase-wrapping (detailed in the preceding subsection), careful treatment is required to ensure we obtain statistics that are representative of the true distribution. We discuss this in the following section.

As a next step, we formulate a model relating parameters of interest to the data:

$$\mathcal{G}_f(k_{x_1}, k_{x_2}; \Delta\vec{r}) = \vec{k}(f) \cdot \Delta\vec{r} + \xi, \qquad \xi \sim \mathcal{N}\left(0, \sigma^2_{\delta\Theta_f}\right). \tag{7}$$

Here $\mathcal{G}_f(k_{x_1}, k_{x_2}; \Delta\vec{r})$, the predicted phase-delay, can be related to the wave vector $\vec{k}$ of a propagating mode and the "probe vector" $\Delta\vec{r}$, defined as the vector connecting the probe elements with respect to a user-defined, common axis. In other words, $\mathcal{G}_f((k_{x_1}, k_{x_2}); \Delta\vec{r})$ is the model output for the phase change we expect to observe for a particular probe configuration $\Delta\vec{r}$ given the input parameters (k_{x_1}, k_{x_2}) are the true wave vector components. We note that, for the plasma environment in this work, we have assumed no wave propagation in the azimuthal direction, and thus only perform inference over the radial (k_{x_1}) and axial (k_{x_2}) wavenumbers. To encode measurement noise and uncertainty, we endow the model with Gaussian noise ξ

Copyright 2025 by the Electric Rocket Propulsion Society. All rights reserved.

distributed with zero mean and variance $\sigma^2_{\delta\Theta_f}$ equal to the variance of experimental measurements of $\delta\Theta_f$, i.e. $\sigma^2_{\delta\Theta_f} = \mathbb{V}ar[\delta\Theta_f]$. The corresponding Gaussian likelihood function, given by Eqn. 8, incorporates the mean and variance from all n histograms corresponding to a given frequency.

$$\mathcal{L}_f(\Delta\Theta_f^i | k_{x_1}, k_{x_2}; [\Delta\vec{r}_1 ... \Delta\vec{r}_n]) = \prod_{i=1}^{n} \frac{1}{2\pi\sigma^i_{\delta\Theta_f}} exp\left(-\frac{1}{2}\frac{(\mathcal{G}_f^i(k_{x_1}, k_{x_2}; \Delta\vec{r}_i) - \Delta\Theta_f^i)^2}{(\sigma^2)^i_{\delta\Theta_f}}\right). \tag{8}$$

Here, under the additional assumption of uncorrelated observations between all measurement geometries, i.e. the observed data are conditionally independent given model parameters, we define the overall likelihood distribution as the joint probability of Gaussian likelihoods of each probe geometry. In other words, we posit that the true wavenumbers will maximize the product of individual Gaussian likelihoods across all probe geometries. In principle, with a sufficient number of angle and spacing variations, even if the data is aliased in one direction, the particular combination of $\Delta\Theta_f$ associated with the set of probe geometries will be largely unique to one wave vector.

We note here that in this work we elect to use grid search where, for each frequency index, we sweep the input parameters $\theta = k_{x_1}, k_{x_2}$ across a range of wavenumbers to generate a heat map of the likelihood as a function of k_{x_1} and k_{x_2}. For 3D dispersion, MCMC can be used instead for computational efficiency [18][19].

Lastly, we note that the likelihood values can be rescaled to bring out relevant features, for instance, through exponentiation or taking their natural log. Additionally, we have found in this work that a sum of Gaussians provides a better-suited representation of the likelihood to aid in visualizing the topology of resulting PDFs. We adopt these two approaches in this work primarily to gain additional insight from the impact of different probing geometries on the various features and artifacts manifested on the likelihood plots, which would otherwise be obscured when employing a product of Gaussians approach. Critically, since both the sum and product of Gaussians are maximized at the true wavenumbers and both allow equal contribution to the likelihood from each probe geometry, the peaks of the resulting PDFs are coincident. However, we note that the product of Gaussians remains the statistically rigorous method for experiment if visualization of the underlying topology is irrelevant.

E. Extracting histogram statistics

Given the possibility of phase-wrapping, the statistics of dispersion cannot be blindly extracted from phase-delay histograms. We illustrate this with the following, notional example in Fig. 4. Suppose a marginally aliased mode with wavenumber $k \cong k_{max}$ is measured, where its "true" distribution (shown in purple) of phase difference is approximately centered about π. Subject to aliasing, bispectral analysis will instead produce the phase-wrapped phase-delay histogram (orange) with a mean centered about $\approx -k_{max}$. It is evident that if we were to blindly extract statistics from this histogram (orange) without accounting for phase-wrapping, we would mistakenly extract a mean phase of approximately 0 and an erroneously large variance. These statistics would be grossly unrepresentative of the true distribution. In light of this, we adopt the following algorithm to extract close estimates of the true histogram statistics.

1. Set the bin width of the histogram.
2. Take the mode, argmax$[f(\delta\Theta)]$, of the histogram as an estimate for the mean
3. Phase shift the distribution such that argmax$[f(\delta\Theta)]$ is centered about 0 through the following:
   (a) If argmax$[f(\delta\Theta)] > 0$
      i. subtract argmax$[f(\delta\Theta)]$ from all phases ($\delta\Theta$) that satisfy $\delta\Theta \geq$ argmax$[f(\delta\Theta)] - \pi$
      ii. subtract argmax$[f(\delta\Theta)]$ and add 2π to all phases that satisfy $\delta\Theta <$ argmax$[f(\delta\Theta)] - \pi$
   (b) If argmax$[f(\delta\Theta)] < 0$
      i. add $-$argmax$[f(\delta\Theta)]$ to all phases that satisfy $\delta\Theta \leq$ argmax$[f(\delta\Theta)] + \pi$
      ii. add $-$argmax$[f(\delta\Theta)]$ and subtract 2π from all phases that satisfy $\delta\Theta >$ argmax$[f(\delta\Theta)] + \pi$
4. Extract the variance σ^2 of the phase-shifted histogram (green distribution in Fig. 4)

Copyright 2025 by the Electric Rocket Propulsion Society. All rights reserved.

Given sufficient samples of a dominant mode, perturbed by Gaussian noise, the histogram should converge to a Gaussian, a symmetric distribution. The mode of the histograms can thus serve as a proxy for the mean. Using this estimate of the mean, we can phase-shift the distribution such that it is centered about zero per step 3 above. We can then compute the variance of this phase-shifted distribution (green), and we see the shape of which is now much more representative of the true distribution. We show in Tables 1 and 2 a comparison of the estimated statistics of the distributions shown in Fig. 4 with and without conditioning for phase-wrapping. It is evident from these results that computing the statistics without accounting for phase-wrapping leads to significant deviation of the estimated statistics from their true values.

The histogram bin-width is a key hyperparameter in this algorithm and should be selected based on the number of data samples and desired wavenumber resolution. Because we have used the mode as an approximation for the mean, the bin width directly determines wavenumber uncertainty of the estimated mean, i.e. the estimated mean can lie within $\pm\frac{1}{2}\Delta k$, where Δk is bin width, of the true mean. This uncertainty can be decreased by decreasing the bin width; however, this comes at the increased risk of mean estimation error due to spuriously high counts in random bins resulting from measurement noise. This can be mitigated with sufficiently high samples, which should damp out erroneously high bin counts as the histogram converges to a Gaussian. The user must strike a balance, dependent on the number of samples, between wavenumber uncertainty inherent to histogram bin width and noise-driven error associated with overly narrow bins. In this work, we set a phase bin-width of 0.005 radian (200 total bins) corresponding to a wavenumber uncertainty of $\pm 2.24 m^{-1}$. We emphasize that this value is dependent on the signal-to-noise in experiment. An alternative, potentially more robust, approach to mitigating noise without the requirement of hyperparameter tuning would be to fit a Gaussian to the histogram.

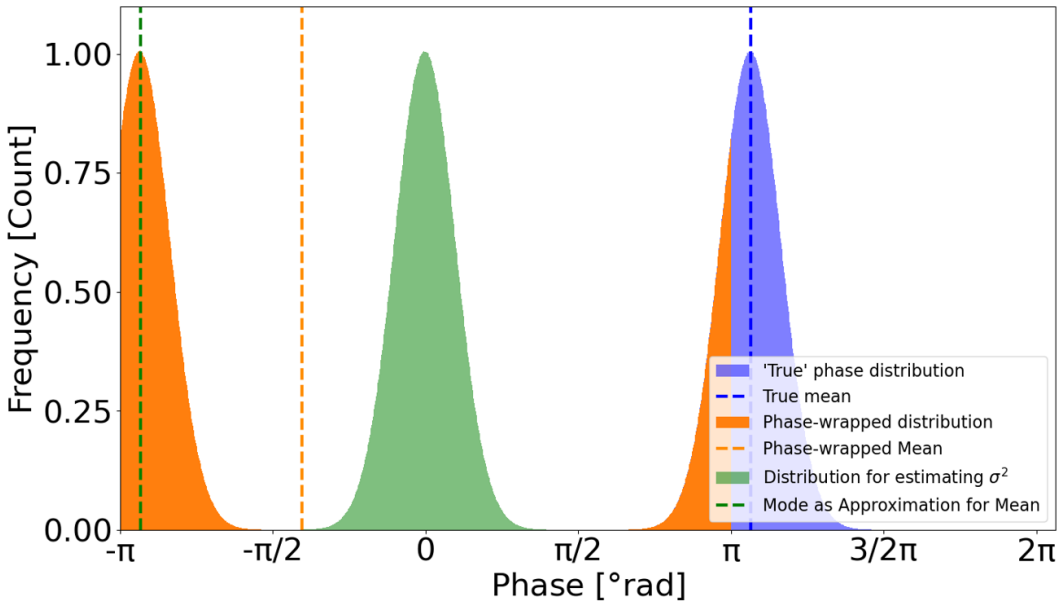

Figure 4: True distribution, phase-wrapped distribution, and distribution used to estimate variance

-	Value	% Err.
True Mean	$\frac{17\pi}{16}$ aliased to $\frac{-15\pi}{16}$	0
Phase-wrapped Mean	-1.274	44.03
Mode (phase-corrected)	-2.928	0.517

Table 1: Comparison of histogram means

-	Value	% Err.
True Variance	$\frac{\pi}{32}$	0
Phase-wrapped variance	6.505	6,525
Phase-shift corrected variance	$\frac{\pi}{32}$	0

Table 2: Comparison of histogram variances

Copyright 2025 by the Electric Rocket Propulsion Society. All rights reserved.

IV. Experimental Apparatus

We outline in this section the experimental configuration and methodology we employ in our work. We first present the test article and facility, followed by an overview of the diagnostic used to measure plasma waves.

A. Hollow cathode test article

The test article shown in Fig. 5 is a lanthanum hexaboride (LaB_6) hollow cathode designed for the 9-kW H9 Hall thruster with a nominal operating current of 15-20 A [20][21]. To induce strong IAT in the plume, we operate the cathode on krypton at a 61.1 A, 22-sccm condition in our test. A water-cooled cylindrical anode placed 25 mm downstream of the cathode orifice sustains the discharge during the test.

B. Facility

We test the H9 cathode in the Cathode Test Facility (CTF). This 0.6 m in diameter by 1 m long vacuum facility (Fig. 6) is pumped by a 135 CFM mechanical roughing pump and a 20" CVI TM500 cryopump with a measured pumping rate of 1500 L/s on Xe. The chamber can achieve a typical base pressure of $\approx 1 \times 10^{-6}$ Torr-N_2. An InstruTech IGM401 Hornet ion gauge is employed to monitor chamber pressure. During testing at 22 sccm of propellant flow, the cryopump sustained a chamber pressure of approximately 235 μT.

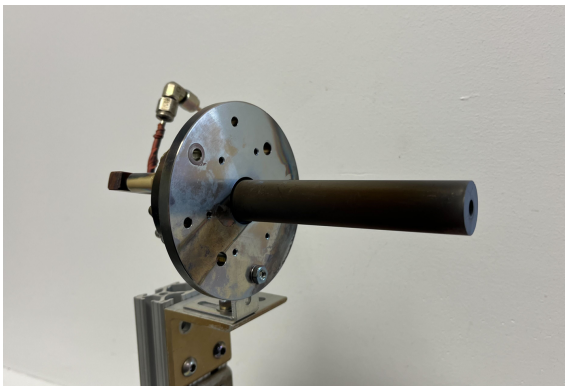

Figure 5: H9 LaB_6 hollow cathode

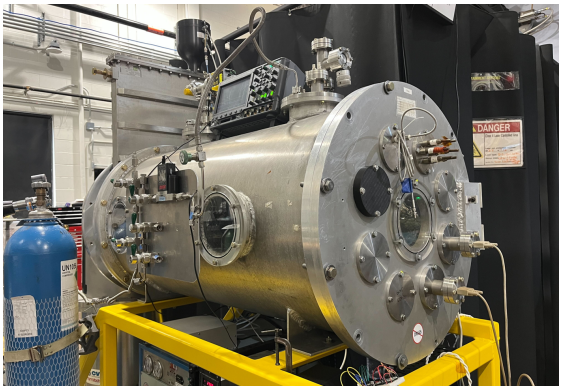

Figure 6: Cathode test facility (CTF)

C. Anti-aliasing wave probes

In principle, for low-amplitude electrostatic waves, ion saturation current fluctuations can be used as a proxy for the plasma potential fluctuations associated with propagating waves [3][12][22]. Assuming electron temperature fluctuations are slow on the timescale of the wave propagation, we can express this relationship as

$$\tilde{\phi}(t) = \frac{T_e}{q} \frac{\tilde{I}_{sat}}{\bar{I}_{DC}}, \tag{9}$$

where $\tilde{I}_{sat}$ denotes the time-varying component of the ion saturation current and $\bar{I}_{DC}$ is the time-averaged component. To measure such fluctuations in plasma, we employ a pair of Langmuir probes biased -37V to ion-saturation mode using batteries. The cylindrical tungsten probe tips measure 0.5 mm in diameter and 2.5 mm in length for a total collection area of 4.12 mm^2. The central probe is placed 15 mm from the cathode keeper orifice with a minimum inter-probe spacing of 3.5 mm. The probes are mounted on two motorized stages that allow for in situ adjustment of probe spacing and angle. A Thorlabs PRMTZ8 motorized precision rotation stage with a bidirectional repeatability of $\pm 0.1^\circ$ is employed to control probe angle, and a Thorlabs Z812 linear actuator with a resolution of 29 nm is used to adjust probe spacing. A pair of Thorlabs KDC101 brushed DC servo motor controllers is used for high-accuracy encoding and control of the two motorized stages. Figs. 7 and 8 show the anti-aliasing probe array and its placement in the experimental arrangement. We show our testing configuration in Fig. 9.

Copyright 2025 by the Electric Rocket Propulsion Society. All rights reserved.

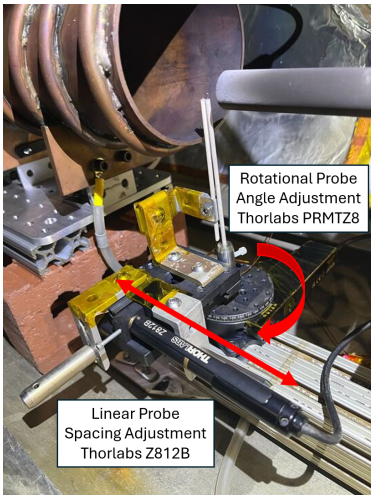

Figure 7: Anti-aliasing probe

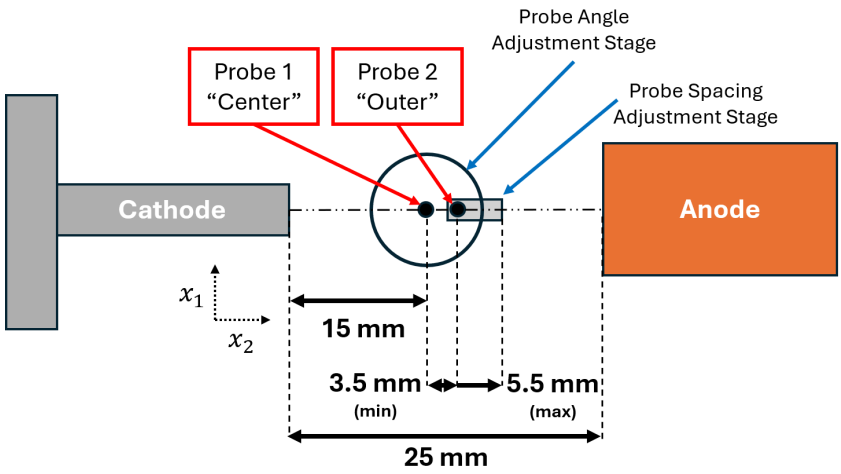

Figure 8: Experimental arrangement schematic

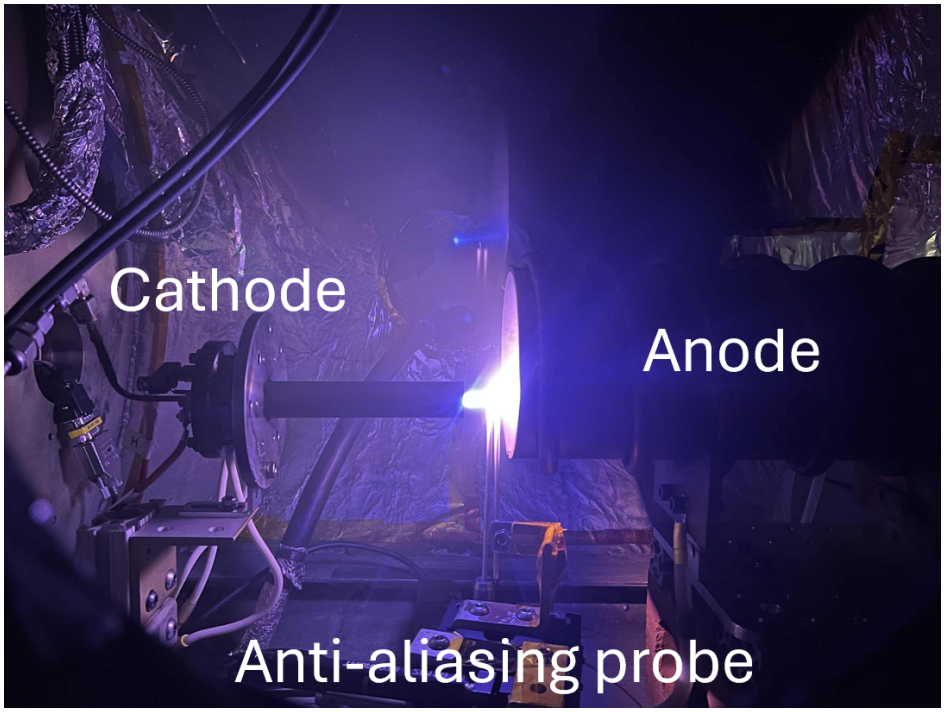

Figure 9: Testing configuration

We collect four datasets using various geometries to examine the effects of spacing and angle step size. The probing geometries are tabulated in Tab. 3 and are shown in Fig. 10. Here, x_2 corresponds to the axial direction, aligned with the longitudinal axis of the cathode, and x_1 corresponds to the radial direction. We use the 3.5 mm probe spacing and 0 ° probe angle datasets from each of the four probing geometries for our Beall analysis results in the axial direction, and the 3.5 mm probe spacing and 90 ° probe angle datasets for the radial direction Beall plots.

Copyright 2025 by the Electric Rocket Propulsion Society. All rights reserved.

Analysis Technique	Spacings (mm)	Angles ($^\circ$)
Beall analysis (axial)	3.5	0
Antialiasing analysis: “LALS” (large angle large spacing)	3.5 4, 4.5, 5, 5.5	0, 22.5, 45, 67.5, 90
Antialiasing analysis: “SALS” (small angle large spacing)	3.5 4, 4.5, 5, 5.5	0, 5, 10, 15, 20
Antialiasing analysis: “LASS” (large angle small spacing)	3.5, 3.6, 3.7, 3.8, 3.9	0, 22.5, 45, 67.5, 90
Antialiasing analysis: “SASS” (small angle small spacing)	3.5, 3.6, 3.7, 3.8, 3.9	0, 5, 10, 15, 20

Table 3: Comparison of Beall and Antialiasing probing geometries

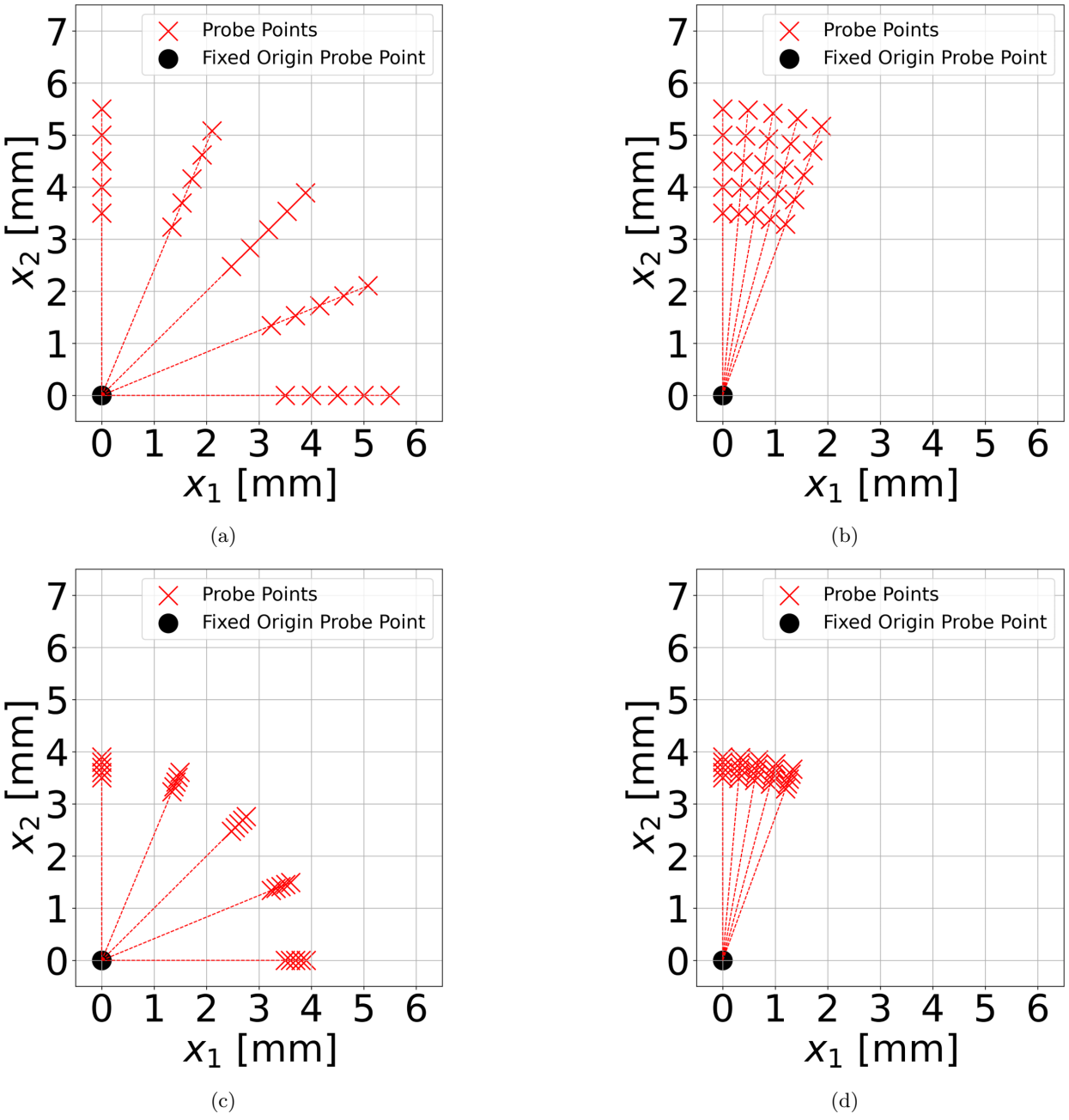

(a) (b) (c) (d)

Figure 10: Antialiasing probing geometries: a) $\Delta\theta = 22.5^\circ, \Delta r = 0.5$ mm LALS Geometry, b) $\Delta\theta = 5^\circ, \Delta r = 0.5$ mm SALS Geometry, c) $\Delta\theta = 22.5^\circ, \Delta r = 0.1$ mm LASS Geometry, d) $\Delta\theta = 5^\circ, \Delta r = 0.1$ mm SASS Geometry

Copyright 2025 by the Electric Rocket Propulsion Society. All rights reserved.

Time-resolved ion-saturation current fluctuations are inferred by measuring the voltage drop across a 100-Ω low-inductance metal foil resistor using a Keysight DSO-X 3024 Oscilloscope. We show the current sensing circuit diagram in Fig.11. The oscilloscope is configured to sample with a temporal resolution of 15 ns, corresponding to a maximum Nyquist frequency of 3.333 MHz. The measured bandwidth of the current sensing circuit is 3.4 MHz, which exceeds the upper bound of the frequency domain relevant to this study. We thus ensure that our collected data is unaffected by signal attenuation. For each probe spacing and angle combination, we acquire 50 current traces, each spanning 960 μs. Each trace is subsequently divided into 64 intervals, resulting in a total of 3200 samples. We then Fourier transform these samples to yield 500 spectral pairs per trace corresponding to a frequency resolution of 6.66 kHz.

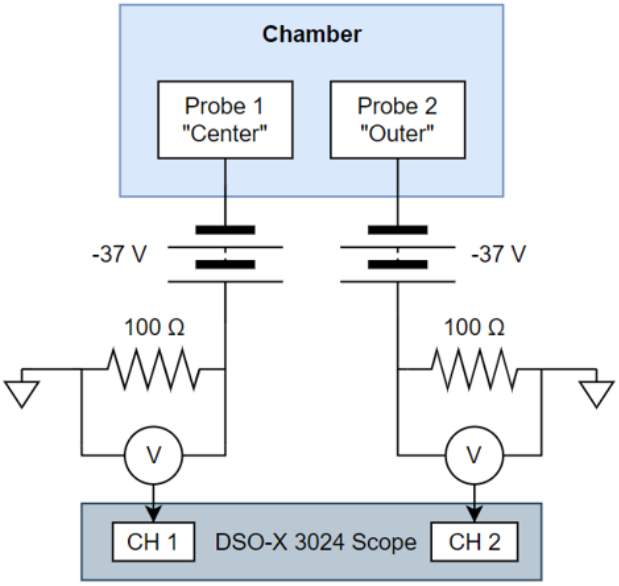

Figure 11: Current sensing circuit diagram [23]

V. Results

We present in this section the primary results of this work. We first show the dispersion obtained via Beall analysis, against which we evaluate our anti-aliasing analysis results later. Next, we show simulation results as a reference for what we expect our anti-aliasing analysis to produce. Lastly, we show dispersion plots produced by applying our anti-aliasing analysis to experimental data.

A. Experimental Beall analysis results

We show in Fig. 12 Beall plots generated from the 3.5 mm, 0° (axial) probe orientation of each dataset, and in Fig. 13 plots generated from the 3.5 mm, 90° (radial) probe orientation of the LALS and LASS datasets. The wavenumber resolution for all plots is set to $\Delta k = 1.795$ m^{-1}, corresponding to a wavelength resolution of approximately 7 μm, such that the axes achieve the same degree of discretization (i.e. the histogram has an equal number of frequency bins as wavenumber bins). To aid in visualization, we plot the natural log of the Beall intensity factor, $S(f, k)$.

There are three notable features that emerge from the Beall plots. First, we note the largely linear dispersion in both the axial and radial direction, which suggests that IAT is the dominant instability present in the plume with modes propagating at up to 2.5 MHz. A comparison between the axial and radial dispersion shows that the axial dispersion extends to much higher wavenumbers, indicating that the wave propagation is primarily axial. The finite radial dispersion may be an artifact from the radial projection of axial wavevectors. This suggests either that the 90° wave probing geometries may not be exactly collinear with the exit plane of the cathode orifice, or that the direction of propagation may not truly be entirely radial at the positions probed. We return to this point later for discussion.

The second notable feature is the discontinuity in wave dispersion and abrupt increase in wavenumber uncertainty between frequencies of approximately 0-100 kHz. This can likely be attributed to ion-neutral damping of ion acoustic waves at low frequency as suggested by Jorns et al. [3] and/or the presence of coherent cathode ionization instabilities, studied extensively by Georgin [24], which have been shown to dominate at these low frequencies.

The final feature we note is the presence of aliasing, characterized by the multiple parallel striations in the dispersion plots. We show the manually de-aliased Beall plots in Fig. 14. The slope of the dispersion suggests a group velocity of approximately 5.6 km/s. Allowing for an ion drift velocity of 2.5 km/s, on the order of ion drift velocities measured in these devices [25], the dispersion suggests an electron temperature of 8.5 eV. Although this value is on the higher end of probe measurements, it is on the order of electron

Copyright 2025 by the Electric Rocket Propulsion Society. All rights reserved.

temperatures in these devices recently measured using incoherent Thomson scattering [26]. The datasets were taken over the course of 6 hours. Furthermore, we operated the cathode at a lower current condition of 15A on 15 sccm of Krypton for 0.5 and 1.5 hours between datasets. We attribute minor qualitative differences between the Beall plots to thermal drift and possible hysteresis effects in switching between the high current and low current modes.

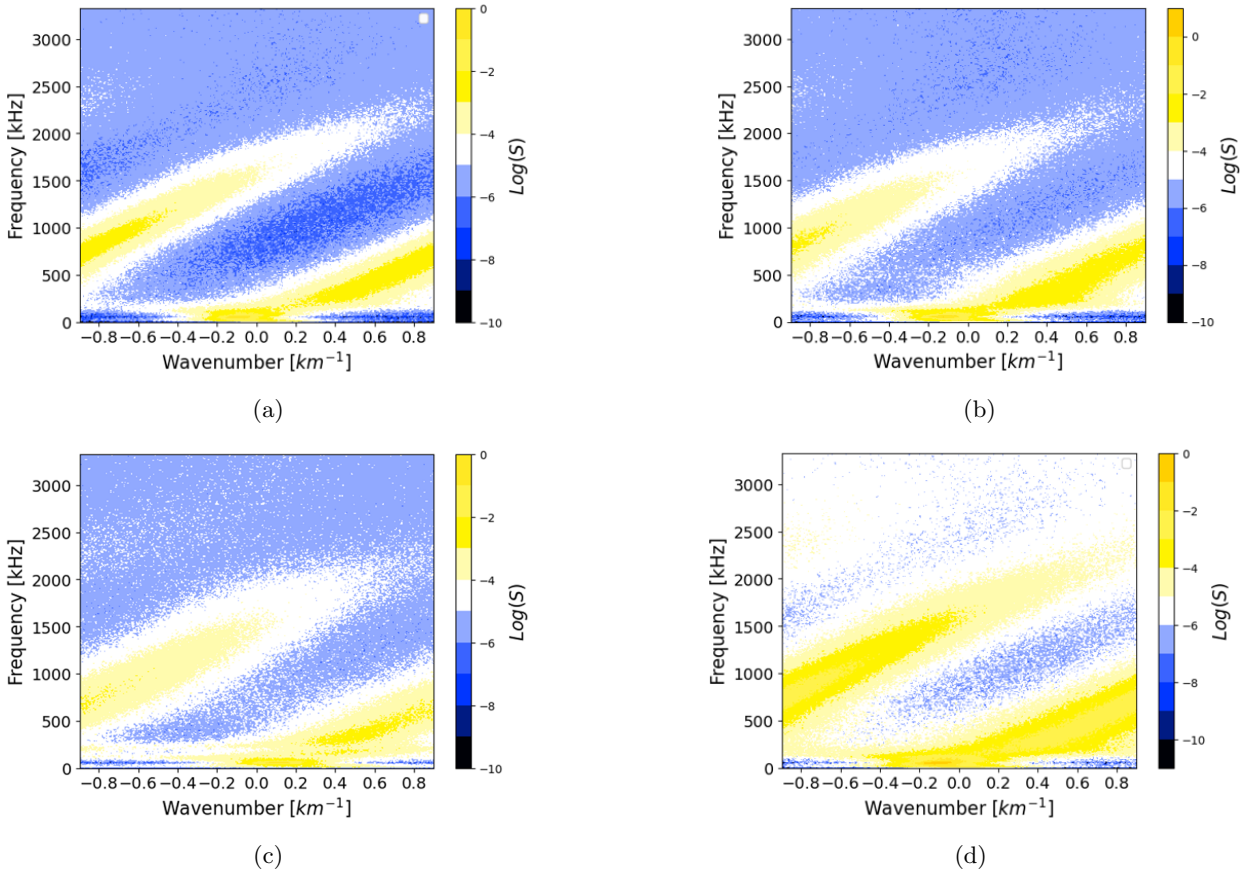

Figure 12: Axial Beall analysis results at 3.5 mm probe spacing: a) $\Delta\theta = 22.5°, \Delta r = 0.5$ mm LALS dataset, b) $\Delta\theta = 5°, \Delta r = 0.5$ mm SALS dataset, c) $\Delta\theta = 22.5°, \Delta r = 0.1$ mm LASS dataset, d) $\Delta\theta = 5°, \Delta r = 0.1$ mm SASS dataset

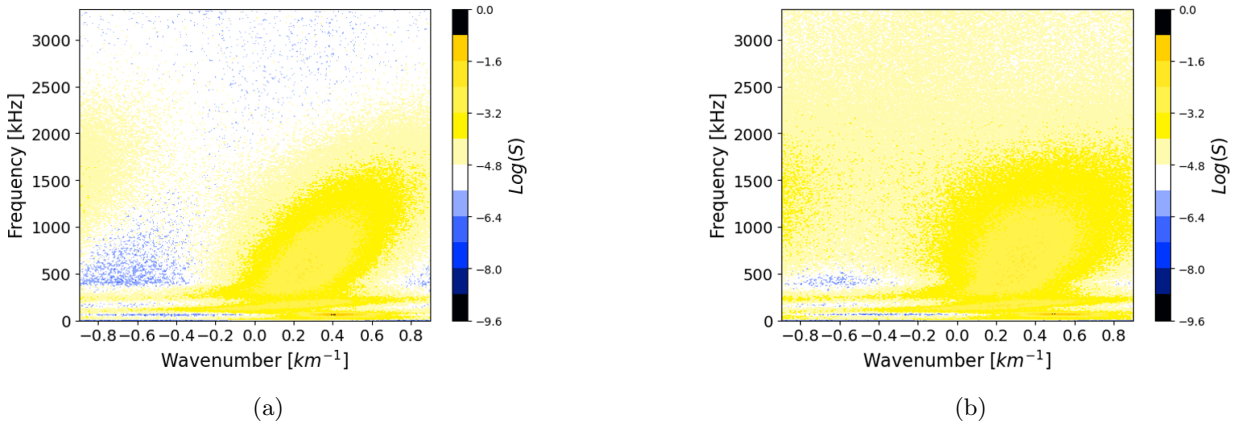

Figure 13: Radial Beall analysis results at 3.5 mm probe spacing: a) $\theta = 90°, r = 3.5$ mm LALS dataset, b) $\theta = 90°, r = 3.5$ mm LASS dataset

Copyright 2025 by the Electric Rocket Propulsion Society. All rights reserved.

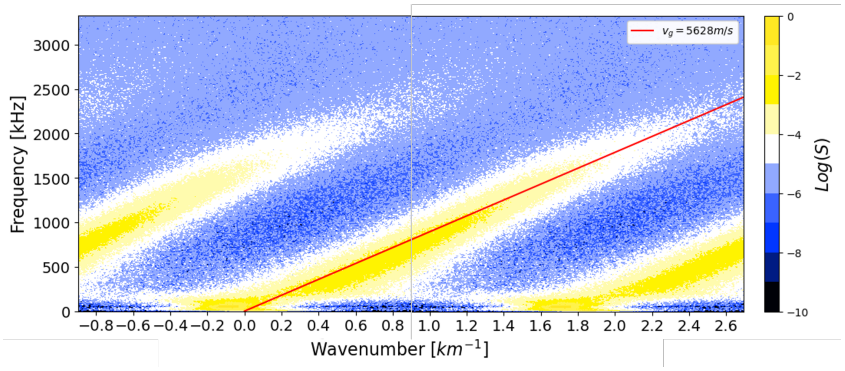

(a)

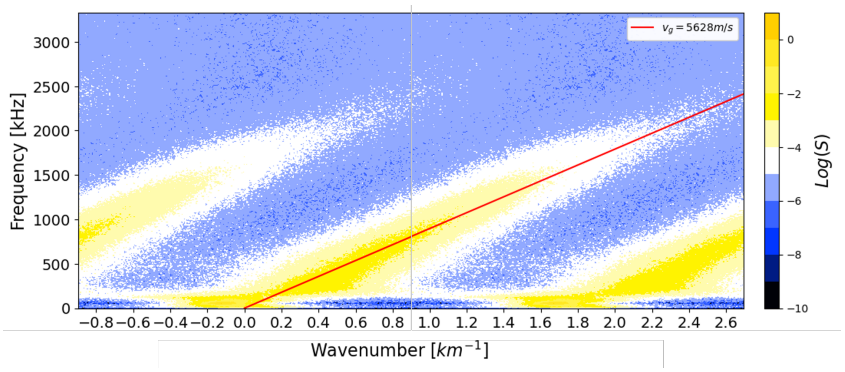

(b)

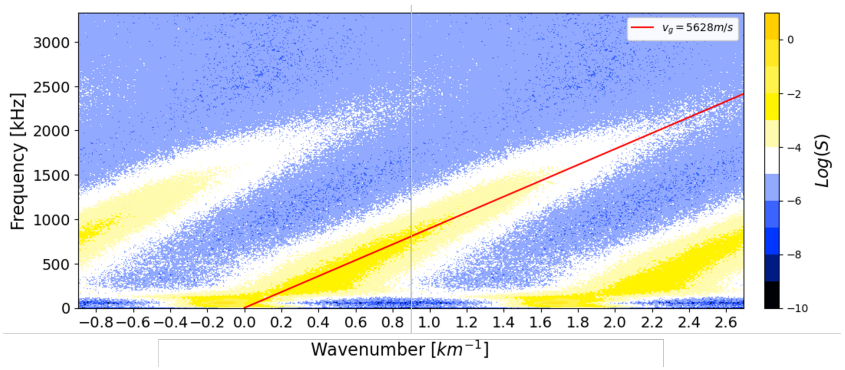

(c)

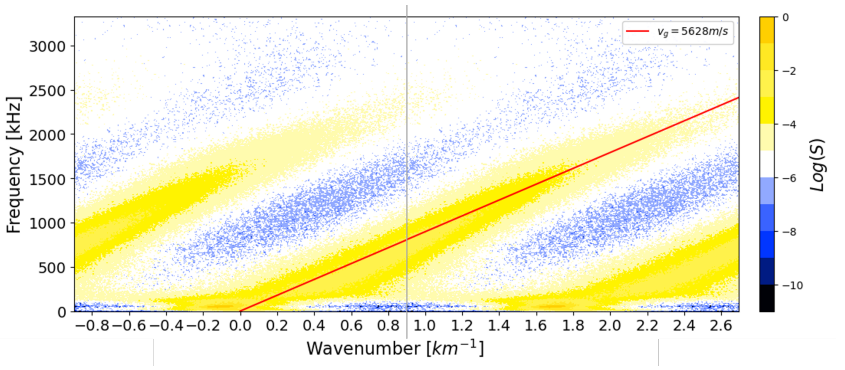

(d)

Figure 14: Manually de-aliased Beall analysis rsults showing approximate group velocity of IAT: a) $\Delta\theta = 22.5°, \Delta r = 0.5$ mm LALS dataset, b) $\Delta\theta = 5°, \Delta r = 0.5$ mm SALS dataset, c) $\Delta\theta = 22.5°, \Delta r = 0.1$ mm LASS dataset, d) $\Delta\theta = 5°, \Delta r = 0.1$ mm SASS dataset

Copyright 2025 by the Electric Rocket Propulsion Society. All rights reserved.

B. Experimental anti-aliasing results: axial dispersion

We show in Figs. 15 and 16 plots of the axial and radial dispersion, respectively, inferred using anti-aliasing analysis on experimental data. The likelihood values shown here have been raised to the third power during post-processing to aid in visualization. There are a few features of note in these results. First, we see that all geometries exhibit anti-aliasing properties, with the highest intensity regions following the theoretical dispersion inferred from Beall analysis results. These plots demonstrate that the anti-aliasing technique is able to resolve sub-millimeter modes.

Next, out of the four sets of probing geometries, the small-angle, small-spacing dataset appears to exhibit the worst performance. However, we see that the wavenumber uncertainty is significantly reduced in the region corresponding to the 3.5 mm probe spacing (0.9 km^{-1}), characterized by a convergence of the intensity to relatively narrow frequency/wavenumber bands around the spatial harmonics of this spacing. We observe this phenomenon to some extent in the LASS dataset as well. We posit that this can be attributed to the reduced "uniqueness" of data gained from the closely spaced probing geometries: there is a wealth of data taken close to 3.5 mm, which drastically decreases the uncertainty at wavenumbers corresponding to this probe spacing. This appears to come at the expense of increased uncertainty across other wavenumbers, as evident from the comparatively higher-intensity content in regions outside of the true dispersion.

Lastly, we note that there are similar features between the dispersion inferred from anti-aliasing analysis and manually de-aliased Beall plots. There appear to be parallel striations with reducing intensity as wavenumber increases. This suggests the likelihood model identifies these harmonics as candidates that *could* explain the data. In effect, our method performs automatic de-aliasing - previously carried out manually - with the clear advantage that the intensity is maximized at the true dispersion, highlighting it as the most probable explanation.

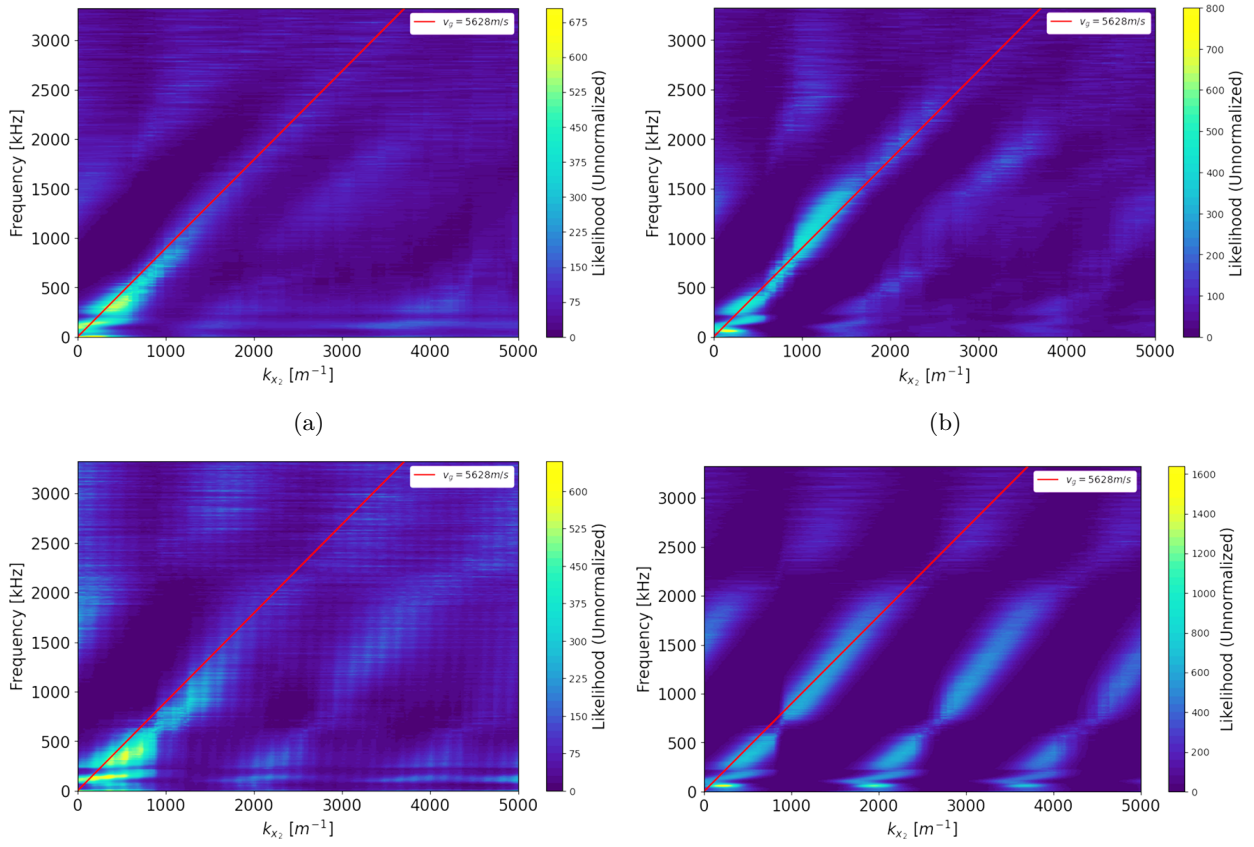

Figure 15: Anti-aliased axial dispersion of experimental data: a) $\Delta\theta = 22.5°, \Delta r = 0.5$ mm LALS dataset, b) $\Delta\theta = 5°, \Delta r = 0.5$ mm SALS dataset, c) $\Delta\theta = 22.5°, \Delta r = 0.1$ mm LASS dataset, d) $\Delta\theta = 5°, \Delta r = 0.1$ mm SASS dataset

Copyright 2025 by the Electric Rocket Propulsion Society. All rights reserved.

C. Experimental anti-aliasing results: radial dispersion

Next, we see from the radial dispersion results that the LALS and LASS datasets predict negligible radial dispersion, with likelihood content concentrated near 0 km^{-1}, aside from what appears to be a coherent mode at low wavenumbers. This can likely be attributed to the ionization mode discussed in the preceding section. The finite, positive radial wavenumber of this mode suggests it may propagate radially outward. In contrast, however, the SALS and SASS datasets suggest a much higher wavenumber for the ionization mode as well as another global mode existing at 1500 kHz near 0 km^{-1}. Critically, none of these results appear to agree qualitatively with the radial Beall results. We return to this point in the discussion section.

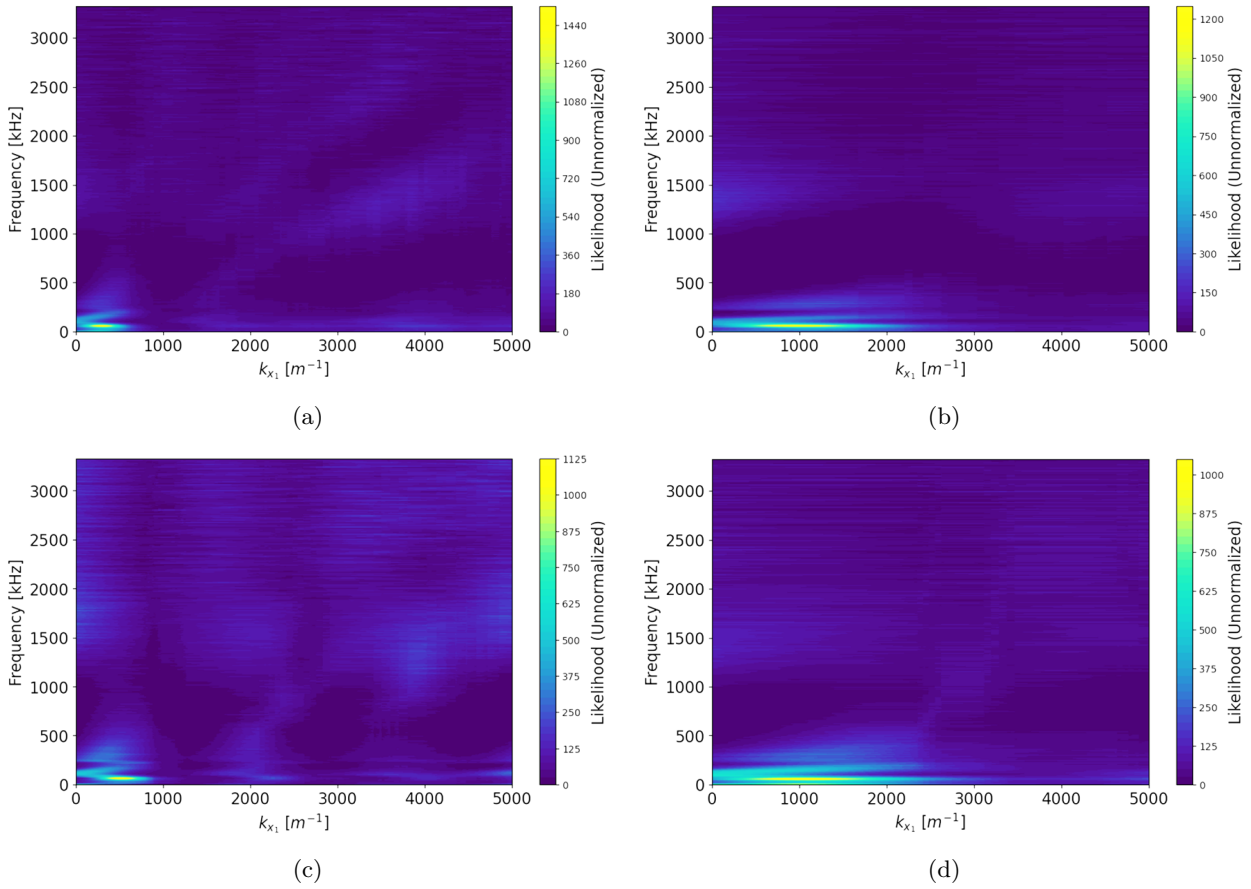

Figure 16: Anti-aliased radial dispersion of experimental data: a) $\Delta\theta = 22.5°, \Delta r = 0.5$ mm LALS dataset, b) $\Delta\theta = 5°, \Delta r = 0.5$ mm SALS dataset, c) $\Delta\theta = 22.5°, \Delta r = 0.1$ mm LASS dataset, d) $\Delta\theta = 5°, \Delta r = 0.1$ mm SASS dataset

D. Experimental anti-aliasing results: inference of wavevector magnitude and direction

Having obtained the PDFs for both the axial and radial directions of dispersion, we can now easily obtain estimates for the wavevector magnitude and direction. We can directly compute the PDF of wavevector magnitude

$$P(r) = \iint\limits_{r \leq \sqrt{x_1^2 + x_2^2} \leq r + dr} P(x_1)\, P(x_2)\, dx_1\, dx_2. \tag{10}$$

Here we integrate the joint likelihood of x_1 and x_2, $P(x_1)$ and $P(x_2)$, respectively, that satisfies $r \leq \sqrt{x_1^2 + x_2^2} \leq r + dr$. In other words, we are tallying the joint likelihood of all combinations of x_1 and x_2 that result in each value of r. This is difficult to integrate in Cartesian coordinates, so we will instead leverage a polar coordinate transform of the above integral to

Copyright 2025 by the Electric Rocket Propulsion Society. All rights reserved.

$$P(r) = \int_0^{2\pi} r\, P\big(r\cos\theta\big)\, P\big(r\sin\theta\big)\, d\theta. \tag{11}$$

Here we have performed the substitutions $x_1 = rcos(\theta)$ and $x_2 = rsin(\theta)$. We can obtain a similar PDF of the direction of wave propagation

$$P(\phi) = \int_0^{\infty} r\, P\big(r\cos\phi\big)\, P\big(r\sin\phi\big)\, dr, \tag{12}$$

where we have now defined ϕ as the angle of the wavevector with respect to the radial axis (0° is along the radial axis).

We show in Fig. 17 the inferred wavevector magnitude and direction. The wavevector magnitude plot (Fig. 17a) agrees well with the manually de-aliased Beall plot results, assuming the wave propagation is primarily axial. However, some high intensity regions are present in the region between 2000 - 5000 m^{-1} and 500 - 2000 kHz, which are notably absent in Beall analysis. This artifact could lead to the erroneous conclusion that there is another mode propagating in the plasma at these wavenumbers and frequencies that is distinct from IAT. Perhaps more critically, the wavevector direction plot (17b) appears to be in gross disagreement with conclusions one might draw about the direction of propagation from Beall analysis. Given the largely axial wave propagation, we expect high probability near $\phi = 90°$, but instead observed a highly non-physical spread of probability across many angles. We posit this can largely be attributed to non-optimal probing geometries leading to poor estimates for the radial dispersion results and thus for wavevector direction as well. We elaborate on this point in the discussion.

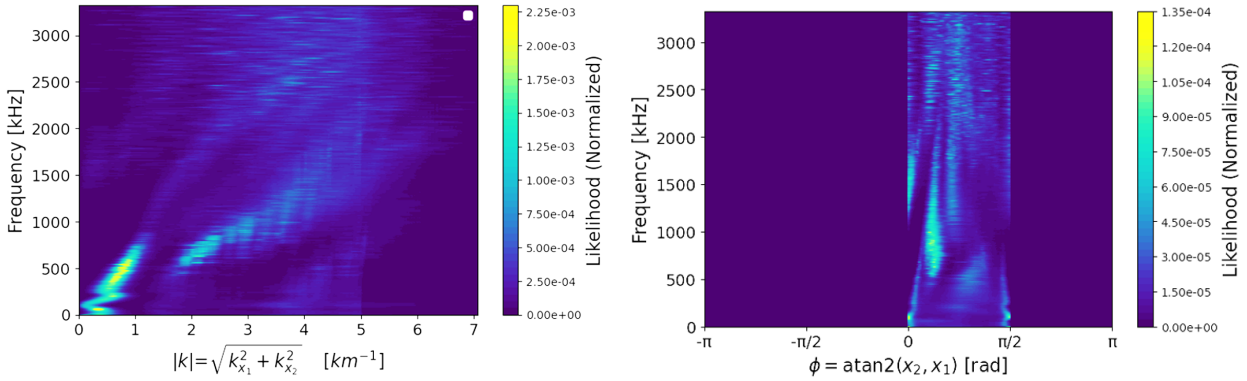

(a) (b)

Figure 17: Experimental dispersion magnitude and direction plots for LALS dataset: a) Wavevector magnitude likelihood, b) Wavevector direction likelihood

E. Summary of results

We briefly summarize here the key insights from this section. First, for the axial direction, we observe aliasing of an ion acoustic-like dispersion, inferred from two-point correlation, characterized by discontinuities in the Beall plots. Comparing these results to multi-point correlation outputs highlights the robust anti-aliasing properties of our Bayesian framework. Next, we find a departure of the multi-point correlation outputs for the radial direction from the dispersion inferred from Beall analysis. Finally, we find non-physical results for the wavevector magnitude and direction generated from the joint distributions of the axial and radial dispersion PDFs, which we posit can be attributed to the poor estimates for dispersion in the radial direction. We return to these points for discussion in the next section.

Copyright 2025 by the Electric Rocket Propulsion Society. All rights reserved.

VI. Discussion

In this section, we discuss departures of our experimental results from the theoretical dispersion. We first present simulation results and compare them to experiment. We then make recommendations on the optimal probing geometries for future experiments leveraging our anti-aliasing framework. Lastly, we discuss the implications of this algorithm for plasma wave analysis, as well as future work.

A. Comparison of experimental results to simulation

A few key questions remained after analyzing our experimental data. First, are the differences observed in the likelihood plots between the varying geometries attributable to artifacts inherent to the algorithm, or were they instead due to real plasma phenomena? Second, what factors contribute to the algorithm's poor performance when inferring the direction of wave propagation?

To answer these two questions, we simulated multiple probing geometries in the presence of propagating plasma waves following the simulation methodology detailed in our earlier work [8]. This approach allows for a direct comparison between algorithm outputs trained on idealized simulation inputs and those produced from experimental data, thereby helping deconvolve algorithm artifacts from real phenomena. Leveraging the experimentally measured dispersion relation described in the preceding section, we simulated IAT modes spanning a frequency range of 0–3.33 MHz with a group velocity of $v_g = 5.6$ km/s. We assume purely axial wave propagation and adjusted the simulation noise level to qualitatively match the signal-to-noise ratio observed in experiment. For each experimental probe orientation (LALS, SALS, LASS, SASS), we generate a corresponding dataset in simulation. Fig. 18 shows Beall analysis performed on the 3.5 mm, 0° (axial) and 90° (radial) simulated datasets. We note a minor simulation glitch manifesting as a horizontal discontinuity at approximately 2250 kHz. This artifact was present in all datasets.

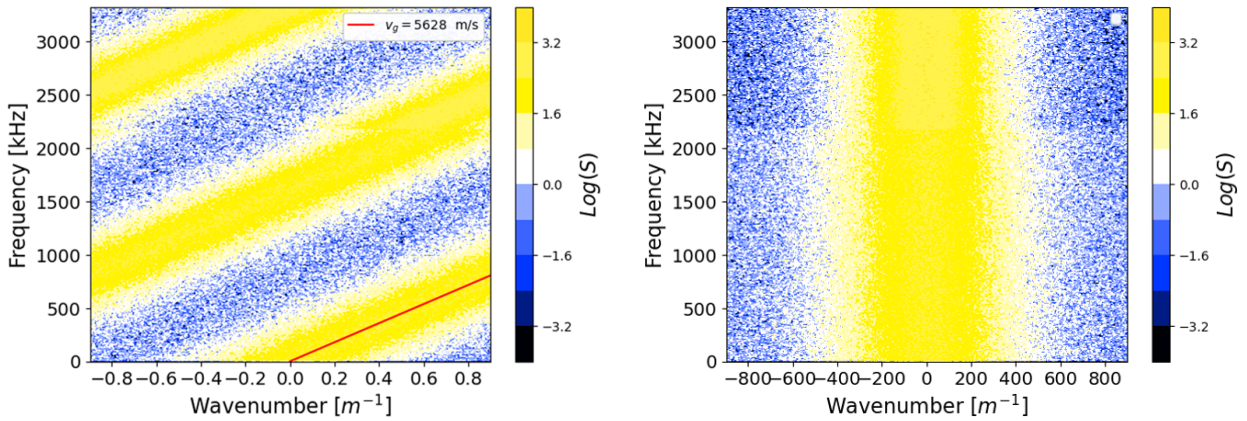

Figure 18: Simulated IAT with group velocity set to experimentally-inferred value: a) Simulated axial dispersion, b) Simulated radial dispersion

Fig. 19 shows plots of the axial dispersion inferred using anti-aliasing analysis for each of the four sets of probing geometries, and Fig. 20 shows the inferred radial dispersion. We observe similar features between the four experimentally-produced likelihood plots in comparison to their simulation counterparts here. Namely, the SASS plot shows the multiple repeating likelihood structures, decreasing in intensity as wavenumber increases. Additionally, the LASS and SASS datasets show decreased wavenumber uncertainty around the wavenumber corresponding to the minimum probe spacing, commensurate with experimental observations. We see that, overall, the LALS dataset appears to produce the likelihood plot with the highest intensity content in the regions corresponding to true wave propagation, consistent with experiment.

From the radial results, we observe similar features to experimental results as well. The LALS and LASS datasets predict negligible radial dispersion, with likelihood content concentrated near 0 km^{-1}. In contrast, the SALS and SASS datasets exhibit apparent linear dispersion with content extending to 2000 km^{-1}, commensurate with the same features observed in their experimental counterparts. As we have shown

Copyright 2025 by the Electric Rocket Propulsion Society. All rights reserved.

from Fig. 18b there should in fact be no radial wave propagation; thus, these artifacts would likely lead us to draw the erroneous conclusion of finite radial wave propagation.

We posit this behavior arises from the absence of true radial measurements in the SALS and SASS configurations, in essence, forcing the algorithm to infer propagation along the radial direction without direct observations. In comparison, the inclusion of radial measurements in LALS and LASS yields likelihood distributions showing negligible radial dispersion, in accordance with the true simulated wave dispersion. In a departure from experimental results, neither the axial nor radial results here appear to show a strong coherent mode with low finite wavenumber. This suggests the features seen between 0-100 kHz in the experimental plots can, in fact, be attributed to the ionization instability discussed earlier.

Having obtained the axial and radial PDFs, we show in Fig. 21 the likelihood plots for wavevector magnitude and direction generated from the LALS dataset for comparison with the experimental result in Fig. 17. The simulated and experimental results exhibit strikingly similar features: both wavevector magnitude plots contain a high-intensity region between wavenumbers of 2000–5000 m^{-1} and frequencies of 500–2000 kHz, and the wavevector direction plots reveal nearly identical likelihood distributions. These consistencies indicate that the algorithm's poor performance arises from limitations inherent to the algorithm or probing geometries rather than from probe effects or from unexpected plasma phenomena, such as cathode mode transitions, corrupting a subset of data. We address why anti-aliasing may be performing sub-optimally in the following subsection.

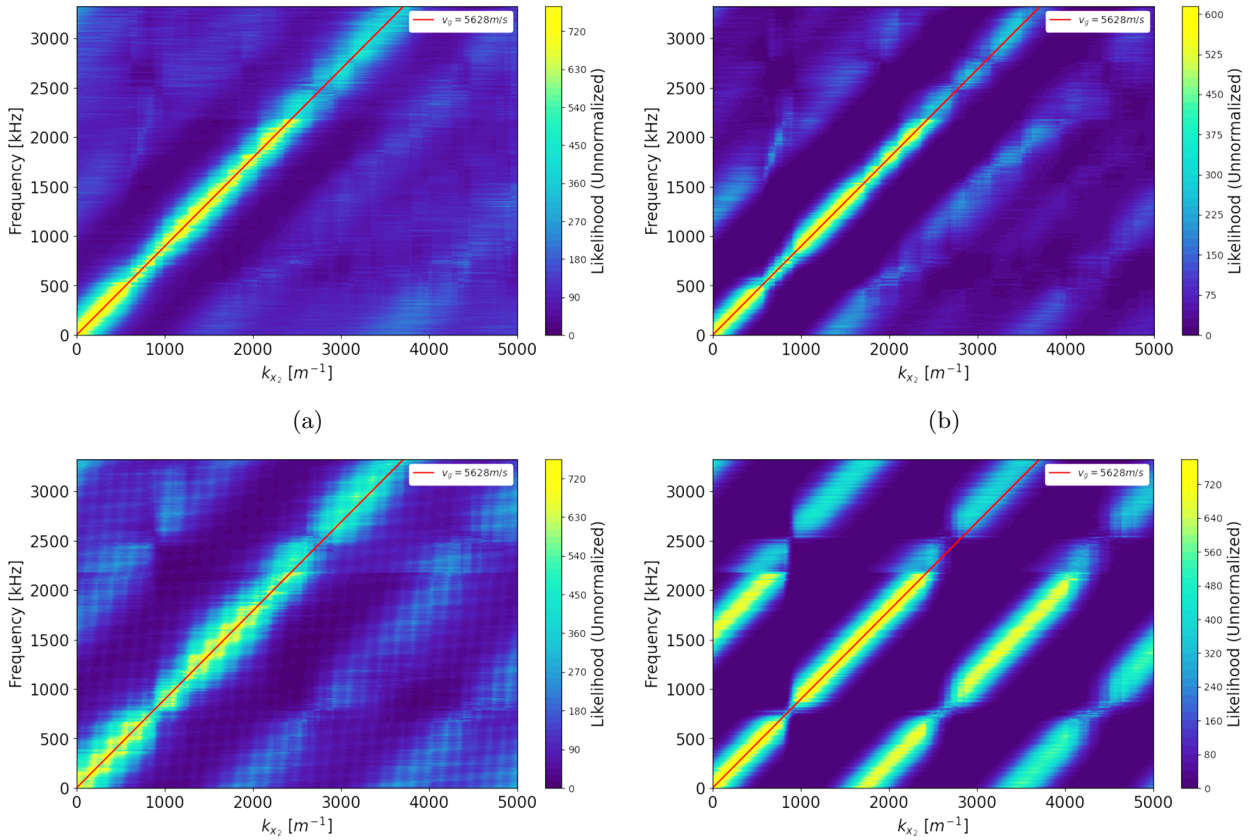

Figure 19: Anti-aliasing applied to axial dispersion of simulated IAT across varying probing geometries: a) $\Delta\theta = 22.5°, \Delta r = 0.5$ mm LALS dataset, b) $\Delta\theta = 5°, \Delta r = 0.5$ mm SALS dataset, c) $\Delta\theta = 22.5°, \Delta r = 0.1$ mm LASS dataset, d) $\Delta\theta = 5°, \Delta r = 0.1$ mm SASS dataset

Copyright 2025 by the Electric Rocket Propulsion Society. All rights reserved.

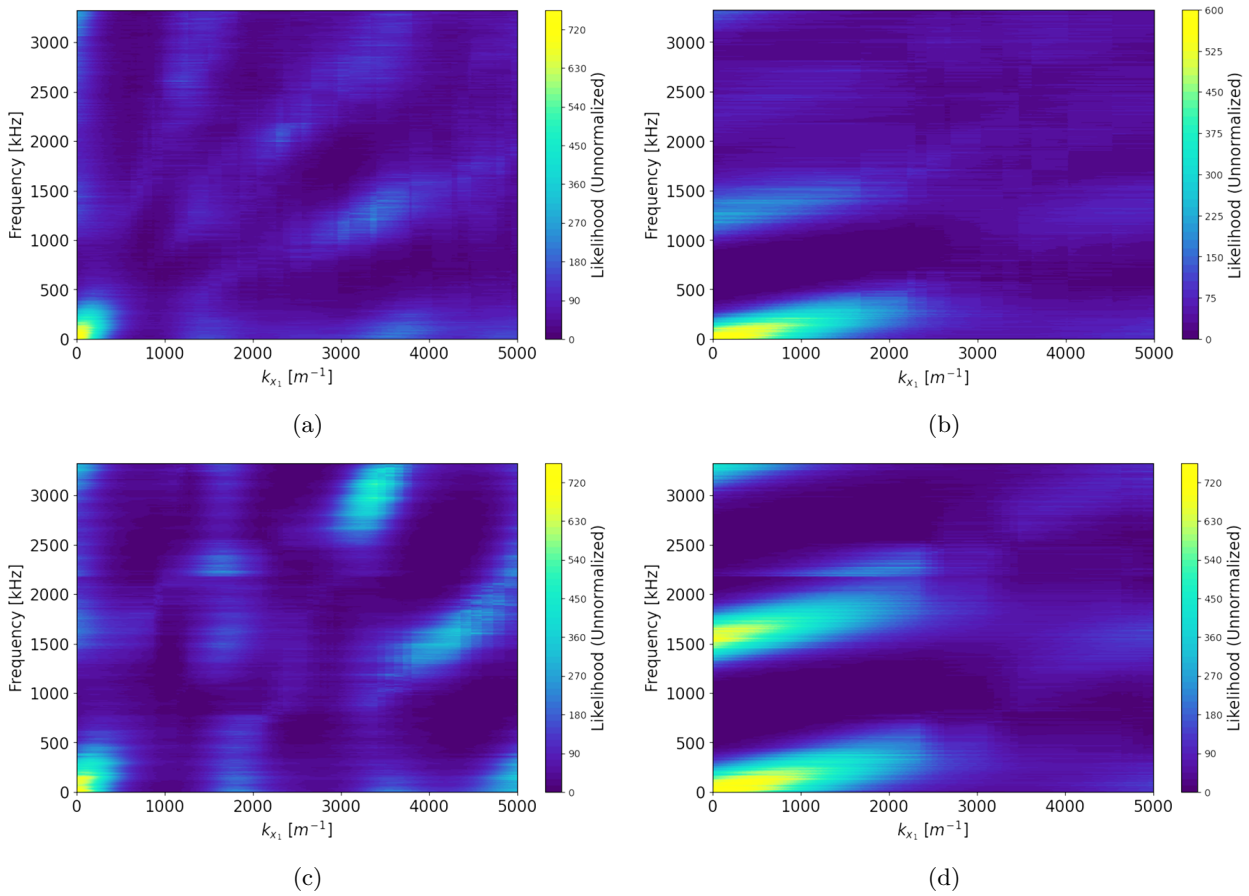

Figure 20: Anti-aliasing applied to radial dispersion of simulated IAT across varying probing Geometries: a) $\Delta\theta = 22.5°, \Delta r = 0.5$ mm LALS dataset, b) $\Delta\theta = 5°, \Delta r = 0.5$ mm SALS dataset, c) $\Delta\theta = 22.5°, \Delta r = 0.1$ mm LASS dataset, d) $\Delta\theta = 5°, \Delta r = 0.1$ mm SASS dataset

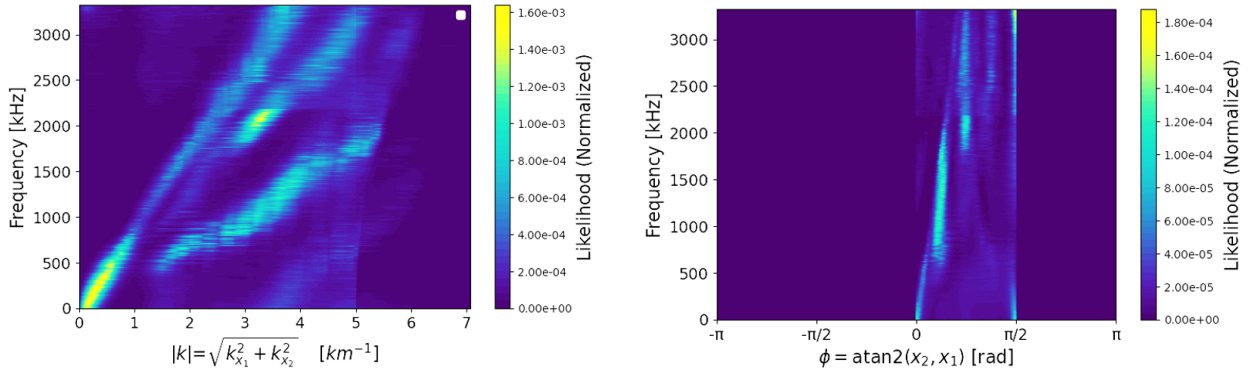

Figure 21: Simulated dispersion magnitude and direction plots for LALS dataset: a) Wavevector magnitude likelihood, b) Wavevector direction likelihood

Copyright 2025 by the Electric Rocket Propulsion Society. All rights reserved.

B. Optimizing probing geometries through simulation

We see from the results presented in the preceding subsection that the simulation results agree qualitatively with the experimental data. From both simulation and experiment, it is evident that some probing geometries may be more effective than others. Therefore, the last outstanding question is: what probing geometries are optimal?

To answer this, we first compare the simulated axial and radial anti-aliasing plots to their Beall counterparts. We see that, while the axial dispersion plots are very similar, the radial plots look very different. Namely, the radial Beall plots show content centered about $k = 0\ km^-1$ extending mostly vertically throughout the entire frequency range. In contrast, the intensity of anti-aliasing plots is highly concentrated with very little content extending up from $k = 0\ km^-1$. We posit it is this discrepancy between the predicted and true radial dispersion that leads to undesirable artifacts in the wavevector magnitude plot and overall poor performance in wavevector direction estimation. This motivates us to examine how radial measurements can be improved.

In principle, good estimates for the axial and radial dispersion should lead to accurate wavevector magnitude and directions predictions. Leveraging the insight gained from Fig. 16 and Fig. 20 that additional measurements along the axis of interest increase the accuracy of predictions, we simulate multiple geometries with many probe points close to the radial axis. We show these results in Fig. 22.

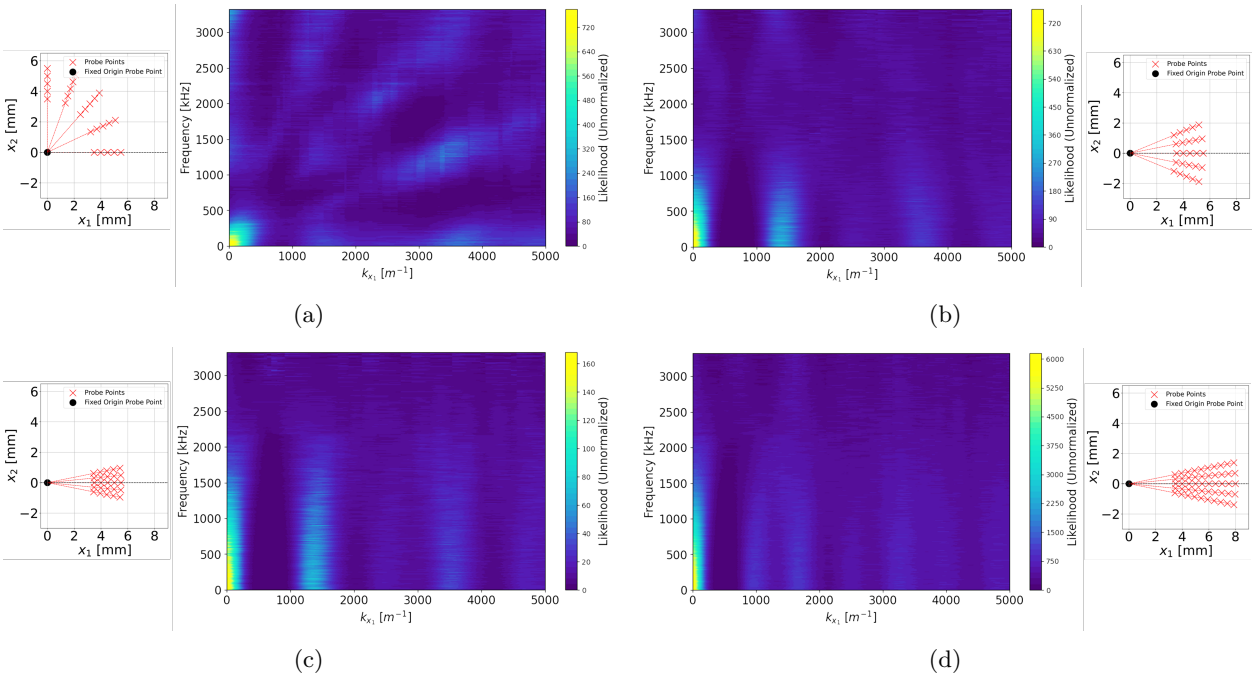

Figure 22: Convergence of simulated radial likelihood to true dispersion given additional measurements along axis: a) $0° \leq \theta \leq 90°$, $\Delta\theta = 22.5°$, $3.5mm \leq r \leq 5.5mm$, $\Delta r = 0.5$ mm config., b) $70° \leq \theta \leq 110°$, $\Delta\theta = 10°$, $3.5mm \leq r \leq 5.5mm$, $\Delta r = 0.5$ mm config., c) $80° \leq \theta \leq 100°$, $\Delta\theta = 5°$, $3.5mm \leq r \leq 5.5mm$, $\Delta r = 0.5$ mm config., d) $80° \leq \theta \leq 100°$, $\Delta\theta = 5°$, $3.5mm \leq r \leq 8mm$, $\Delta r = 0.5$ mm config.

These results confirm that as more data is collected near the axis, the likelihood plots converge to the true dispersion. It is now evident that the optimal probing geometries employ probe spacings spanning a wider range and angular spacings spanning a small range centered about the axis of interest.

With this in mind, we next simulate an example of optimal probing geometries for both the axial and radial directions. We show these results in Fig. 23. We see now that the algorithm outputs closely align with the Beall analysis results shown in Fig. 18. Using these optimized PDFs, we generate the corresponding likelihood plots for the wavevector magnitude and direction, which we show in Fig. 24. These results are physically intuitive, with the magnitude plot following closely the theoretical dispersion, and the direction plot estimating the direction of propagation is likely axial. There are, of course, still some artifacts in these plots, which may be addressed by testing other geometries and tuning the algorithm's hyperparameters.

Copyright 2025 by the Electric Rocket Propulsion Society. All rights reserved.

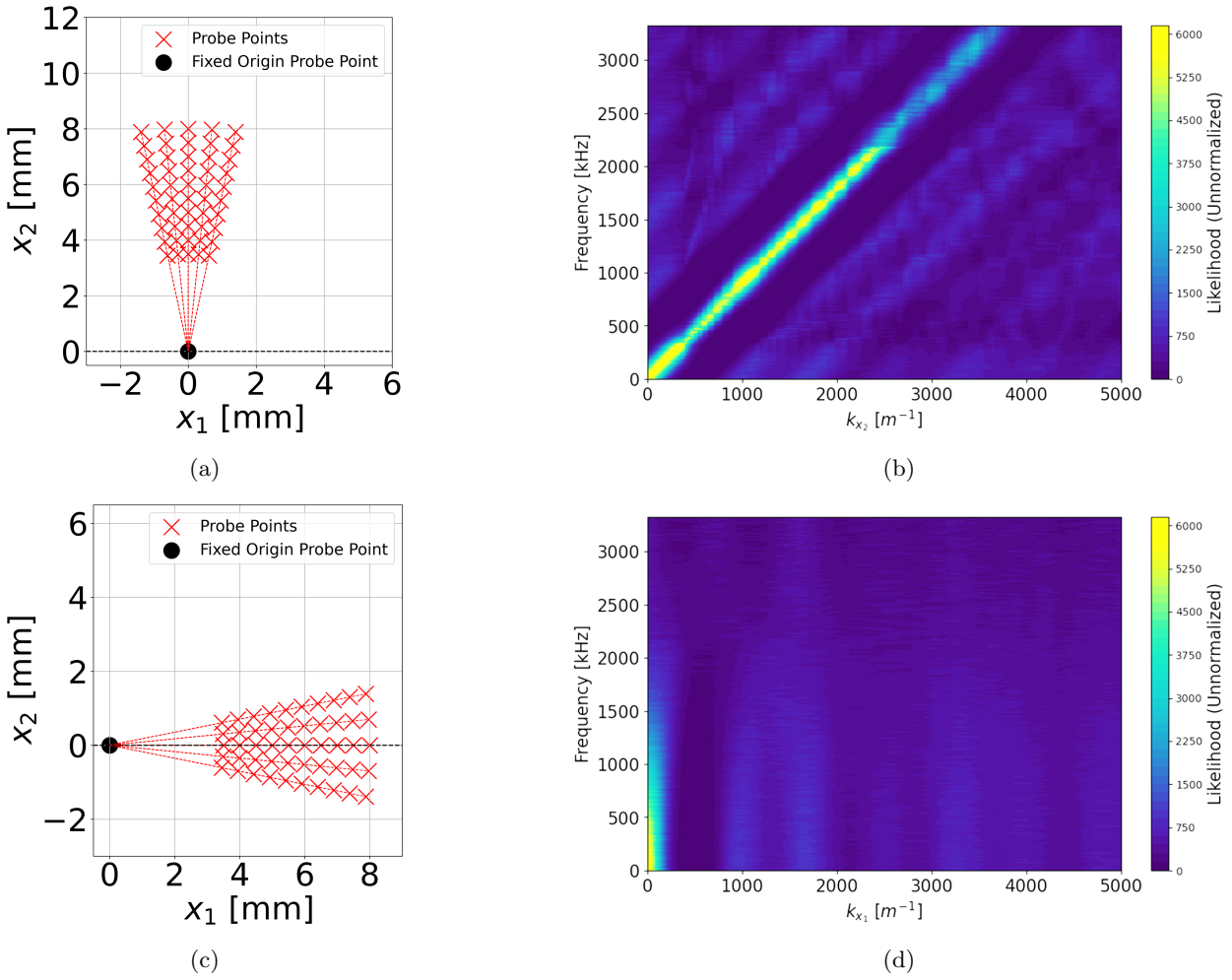

Figure 23: Optimal probing geometries and corresponding axial and radial PDFs: a) Example optimal axial probe geometry, b) Resulting axial dispersion PDF, c) Example optimal radial probe geometry, d) Resulting radial dispersion PDF

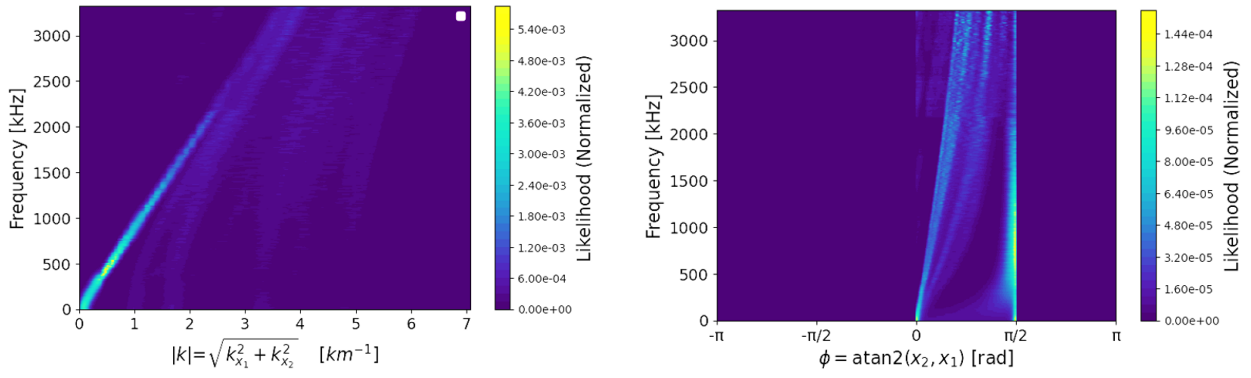

Figure 24: Simulated dispersion magnitude and direction plots given optimal probe geometries: a) Wavevector magnitude likelihood, b) Wavevector direction likelihood

Copyright 2025 by the Electric Rocket Propulsion Society. All rights reserved.

C. Summary of probing geometry best practices

We summarize here a few key insights gained from experimental and simulation regarding optimal probe spacings. First, it appears that using larger probe spacings resulted in likelihood plots with fewer artifacts, suggesting it may be better to leverage probing geometries with greater spatial coverage. However, one critical caveat to note in this approach is that, if the area spanned by probe points is too large, there is the possibility that wave vectors may spatially vary too significantly between probing points. This could lead to erroneous inference of the true direction of wave propagation. Experimental configurations must therefore strike a balance between the area covered by the probe points and the anticipated length scales over which the wave vectors are expected to vary. In the present study, we find that a distance delta of up to 5 mm between probe spacings is a suitable setting for resolving IAT in a hollow cathode plume, but the optimal spacing may change when probing other EP plasmas.

Secondly, we find that attempting to infer dispersion along a given axis while incorporating little experimental data in that direction introduces artifacts in the likelihood plots that are grossly unrepresentative of the true dispersion. We therefore recommend that probe placement include measurements in the vicinity of the axis of interest (see results in preceding subsection). For instance, to resolve radial dispersion, data should be acquired from probe points located near the radial axis. Off-axis measurements serve primarily to mitigate aliasing. As demonstrated in our results, relying predominantly on axial probing geometries to infer radial dispersion leads to spurious conclusions and should therefore be avoided. The relevant axes should ideally be determined by leveraging prior knowledge of the preferred direction of propagation of an instability of interest. In this work, we knew a priori that IAT propagates primarily axially. For modes of interest such as MTSI and LHDI, which have not been experimentally characterized, the most appropriate axes can be determined by the most probable direction of propagation from theory for the respective instabilities, such as given in [7][6]. As a next step, we may then perform a convergence study leveraging various probe configurations to infer the true direction of propagation. It is also possible that taking data at a very large number of spacings and angles, which we did not examine in this present work, obviates the need for any of the aforementioned guesswork.

Lastly, we note that similar algorithm artifacts arise in both simulation and experiment. For future studies employing anti-aliasing probes, there is merit to simulating probe outputs with numerical toy data first. As demonstrated in this work, such simulations can help identify optimal probing geometries and reveal potential artifacts in the likelihood plots that might otherwise lead to erroneous interpretations.

D. Implications for plasma wave analysis and future work

Our findings suggest that this plasma wave analysis technique, in principle, makes possible the detection of waves existing at <1 mm, such as the modified two-stream instability and lower hybrid drift instability. Although these waves have been theorized to dominantly contribute to anomalous ion heating in the vicinity of Hall effect thruster front poles, producing ions with sufficient energies to sputter material from the magnetic poles [7][6], their experimental confirmation has remained elusive, largely due to the historical spatial bandwidth limitations of physical probes. We have shown in this work that the anti-aliasing analysis technique addresses this shortfall, thus greatly expanding the accessible wavelength regime of probe-based diagnostics.

It is important to note that, although the results presented in this work show promise, MTSI and LHDI are inherently 3-dimensional plasma waves. There remains a need to implement the third axis of probing to allow inference of the full 3D wave vectors of these instabilities. Furthermore, we acknowledge the perturbative nature of physical probes. Plasma instabilities are sensitive to local plasma parameters. It is possible that at the regions of high relative plasma density in the near-field plume of a Hall thruster, where MTSI and LHDI are expected to propagate, probe perturbations may obfuscate the true wave dispersion. Nonetheless, we posit that this technique can be readily extended to optical techniques, provided that time-resolved signals linked to plasma density fluctuations can be obtained at multiple locations. Such measurements may be achieved with a combination of LIF and passive high-speed imaging [27].

Copyright 2025 by the Electric Rocket Propulsion Society. All rights reserved.

VII. Conclusion

In this work, we experimentally validated an anti-aliasing plasma wave analysis technique on IAT in a hollow cathode plume. A comparison of the experimental results to two-point correlation Beall analysis highlights the robust anti-aliasing properties of the new technique. We find good agreement between Beall analysis and anti-aliasing analysis for the primary direction of wave propagation (axial), but observe some departure between the two techniques for the radial direction. We next investigate confounding factors leading to this discrepancy by modeling our experimental probe configurations in simulation. This approach allowed us to deconvolve probe effects and real experimental phenomena from artifacts inherent to the algorithm. We find good agreement between simulation and experimental results, which confirms that the disagreement between the two methodologies arises from algorithm-specific factors rather than probe perturbations or other real phenomena. A follow-up investigation of various simulated probing geometries revealed that the algorithm is sensitive to the particular probing geometries employed. We then make recommendations on the ideal probing geometries based on these findings. Finally, we discuss the planned and potential extension of this work. Overall, our results suggest that the spatial anti-aliasing analysis technique can enable measurements of small-length scale waves thought to be dominantly responsible for Hall thruster pole erosion, such as LHDI and MTSI, which historically have been inaccessible due to aliasing.

Acknowledgments

This work was supported by NASA under a Space Technology Graduate Research Opportunity (NSTGRO) Fellowship (Grant 80NSSC24K1331), the University of Michigan Rackham Graduate School under the Rackham Merit Fellowship (RMF), and the U.S. Department of Energy, Office of Science, Office of Fusion Energy Sciences, under the Early Career Research Program Award, DE-SC0022988.

Copyright 2025 by the Electric Rocket Propulsion Society. All rights reserved.

References

[1] J. D. Frieman, H. Kamhawi, P. Y. Peterson, D. A. Herman, J. H. Gilland, and R. R. Hofer, "Completion of the long duration wear test of the nasa hermes hall thruster," in (AIAA Propulsion and Energy 2019 Forum), AIAA Propulsion and Energy 2019 Forum. 2019. DOI: 10.2514/6.2019-3895.

[2] A. Sengupta, J. R. Brophy, J. R. Anderson, C. E. Garner, K. K. de Groh, and T. Karniotis, "An overview of the results from the 30,000 hr life test of deep space 1 flight spare ion engine," *40th AIAA/ASME/SAE/ASEE Joint Propulsion Conference and Exhibit*, 2004. DOI: 10.2514/6.2004-3608.

[3] B. A. Jorns, I. G. Mikellides, and D. M. Goebel, "Ion acoustic turbulence in a 100-a lab6 hollow cathode," *Phys. Rev. E*, vol. 90, no. 6, 2014. DOI: 10.1103/PhysRevE.90.063106.

[4] S. Tsikata, N. Lemoine, V. Pisarev, and D. M. Grésillon, "Dispersion relations of electron density fluctuations in a hall thruster plasma, observed by collective light scattering," *Physics of Plasmas*, vol. 16, no. 3, p. 033 506, Mar. 2009, ISSN: 1070-664X. DOI: 10.1063/1.3093261.

[5] S. Tsikata, K. Hara, and S. Mazouffre, "Characterization of hollow cathode plasma turbulence using coherent thomson scattering," *Journal of Applied Physics*, vol. 130, no. 24, p. 243 304, Dec. 2021, ISSN: 0021-8979. DOI: 10.1063/5.0071650.

[6] I. G. Mikellides and A. L. Ortega, "Growth of the modified two-stream instability in the plume of a magnetically shielded hall thruster," *Physics of Plasmas*, vol. 27, no. 10, p. 100 701, Oct. 2020, ISSN: 1070-664X. DOI: 10.1063/5.0020075.

[7] I. G. Mikellides and A. Lopez Ortega, "Growth of the lower hybrid drift instability in the plume of a magnetically shielded hall thruster," *Journal of Applied Physics*, vol. 129, no. 19, p. 193 301, May 2021, ISSN: 0021-8979. DOI: 10.1063/5.0048706.

[8] M. F. Liu and B. A. Jorns, "Anti-aliasing technique for inferring dispersion of short-wavelength instabilities in electric propulsion devices," *AIAA SCITECH 2025 Forum*, 2025. DOI: 10.2514/6.2025-1293.

[9] V. Y. Bychenkov, V. P. Silin, and S. A. Uryupin, "Ion-acoustic turbulence and anomalous transport," *Physics Reports*, 1988. DOI: 10.1016/0370-1573(90)90122-i.

[10] T. H. Stix, "Waves in plasmas: Highlights from the past and present," *Physics of Fluids B: Plasma Physics*, vol. 2, no. 8, pp. 1729–1743, Aug. 1990. DOI: 10.1063/1.859444.

[11] D. G. Swanson, "Plasma waves (2nd edition)," *Plasma Physics and Controlled Fusion*, 2003. DOI: 10.1088/0741-3335/45/6/701.

[12] S. E. Cusson, B. Jorns, and A. D. Gallimore, "Ion acoustic turbulence in the hollow cathode plume of a hall effect thruster," *2018 Joint Propulsion Conference*, 2018. DOI: 10.2514/6.2018-4509.

[13] A. L. Ortega, B. A. Jorns, and I. G. Mikellides, "Hollow cathode simulations with a first-principles model of ion-acoustic anomalous resistivity," *Journal of Propulsion and Power*, vol. 34, no. 4, pp. 1026–1038, 2018. DOI: 10.2514/1.B36782.

[14] J. M. Beall, Y. C. Kim, and E. J. Powers, "Estimation of wavenumber and frequency spectra using fixed probe pairs," *Journal of Applied Physics*, 1982. DOI: 10.1063/1.331279.

[15] Z. A. Brown and B. A. Jorns, "Growth and saturation of the electron drift instability in a crossed field plasma," *Phys. Rev. Lett.*, vol. 130, no. 11, Mar. 2023. DOI: 10.1103/PhysRevLett.130.115101.

[16] I. G. Mikellides and A. L. Ortega, "The dispersion of the modified two-stream and lower hybrid drift instabilities in the near-pole plume of a magnetically shielded hall thruster," *AIAA Propulsion and Energy 2021 Forum*, 2021. DOI: 10.2514/6.2021-3416.

[17] Z. Brown and B. Jorns, "Experimental measurements of the contribution of plasma turbulence to anomalous collision frequency in a hall thruster," *AIAA Propulsion and Energy 2021 Forum*, 2021. DOI: 10.2514/6.2021-3415.

[18] W. K. Hastings, "Monte carlo sampling methods using markov chains and their applications," *Biometrika*, vol. 57, no. 1, pp. 97–109, Apr. 1970, ISSN: 0006-3444. DOI: 10.1093/biomet/57.1.97.

Copyright 2025 by the Electric Rocket Propulsion Society. All rights reserved.

[19] H. Haario, M. Laine, A. Mira, and E. Saksman, "Dram: Efficient adaptive mcmc," *Statistics and Computing*, 2006. DOI: 10.1007/s11222-006-9438-0.

[20] R. R. Hofer, S. E. Cusson, R. B. Lobbia, and A. D. Gallimore, "The h9 magnetically shielded hall thruster," *35th International Electric Propulsion Conference*, 2017.

[21] S. E. Cusson, R. R. Hofer, R. B. Lobbia, B. A. Jorns, and A. D. Gallimore, "Peformance of the h9 magnetically shielded hall thruster," *35th International Electric Propulsion Conference*, 2017. DOI: null.

[22] A. Brown and B. Jorns, "Dispersion relation measurements of plasma modes in the near-field plume of a 9-kw magnetically shielded thruster," *35th International Electric Propulsion Conference*, 2017.

[23] M. F. Liu and B. A. Jorns, "Experimental measurements of the dispersion and growth rate of ion acoustic waves in the plume of a hollow cathode," *38th International Electric Propulsion Conference*, 2024.

[24] M. Georgin, "Ionization instability of the hollow cathode plume," Ph.D. dissertation, University of Michigan, Ann-Arbor, 2020.

[25] B. A. Jorns, C. Dodson, D. M. Goebel, and R. Wirz, "Propagation of ion acoustic wave energy in the plume of a high-current lab6 hollow cathode," *Phys. Rev. E*, vol. 96, no. 2, Aug. 2017. DOI: 10.1103/PhysRevE.96.023208.

[26] P. J. Roberts and B. Jorns, "Characterization of electron mach number in a hollow cathode with thomson scattering," *AIAA SCITECH 2023 Forum*, 2023. DOI: 10.2514/6.2023-0843.

[27] M. P. Georgin, M. Byrne, B. A. Jorns, and A. D. Gallimore, "Passive high-speed imaging of ion acoustic turbulence in a hollow cathode," *53rd AIAA/SAE/ASEE Joint Propulsion Conference*, 2017. DOI: 10.2514/6.2017-4973.

Copyright 2025 by the Electric Rocket Propulsion Society. All rights reserved.